

University of Nebraska - Lincoln

DigitalCommons@University of Nebraska - Lincoln

Kirill Belashchenko Publications

Research Papers in Physics and Astronomy

12-1-2020

Ultrafast spin-currents and charge conversion at $3d-5d$ interfaces probed by time-domain terahertz spectroscopy

T. H. Dang
Universite Paris-Saclay


J. Hawecker
École Normale Supérieure

E. Rongione
Universite Paris-Saclay

G. Baez Flores
University of Nebraska–Lincoln

D. Q. To
Universite Paris-Saclay

Follow this and additional works at: <https://digitalcommons.unl.edu/physicsbelashchenko>

 Part of the [Atomic, Molecular and Optical Physics Commons](#), [Condensed Matter Physics Commons](#), [Engineering Physics Commons](#), [Other Materials Science and Engineering Commons](#), and the [Statistical, Nonlinear, and Soft Matter Physics Commons](#)

Dang, T. H.; Hawecker, J.; Rongione, E.; Baez Flores, G.; To, D. Q.; Rojas-Sanchez, J. C.; Nong, H.; Mangeney, J.; Tignon, J.; Godel, F.; Collin, S.; Seneor, P.; Bibes, M.; Fert, A.; Anane, M.; George, J. M.; Vila, L.; Cosset-Cheneau, M.; Dolfi, D.; Lebrun, R.; Bortolotti, P.; Belashchenko, Kirill; Dhillon, S.; and Jaffrès, H., "Ultrafast spin-currents and charge conversion at $3d-5d$ interfaces probed by time-domain terahertz spectroscopy" (2020). *Kirill Belashchenko Publications*. 37.
<https://digitalcommons.unl.edu/physicsbelashchenko/37>

This Article is brought to you for free and open access by the Research Papers in Physics and Astronomy at DigitalCommons@University of Nebraska - Lincoln. It has been accepted for inclusion in Kirill Belashchenko Publications by an authorized administrator of DigitalCommons@University of Nebraska - Lincoln.

Authors

T. H. Dang, J. Hawecker, E. Rongione, G. Baez Flores, D. Q. To, J. C. Rojas-Sanchez, H. Nong, J. Mangeney, J. Tignon, F. Godel, S. Collin, P. Seneor, M. Bibes, A. Fert, M. Anane, J. M. George, L. Vila, M. Cosset-Cheneau, D. Dolfi, R. Lebrun, P. Bortolotti, Kirill Belashchenko, S. Dhillon, and H. Jaffrès


Ultrafast spin-currents and charge conversion at 3d-5d interfaces probed by time-domain terahertz spectroscopy

Cite as: Appl. Phys. Rev. 7, 041409 (2020); <https://doi.org/10.1063/5.0022369>

Submitted: 22 July 2020 • Accepted: 03 November 2020 • Published Online: 07 December 2020

T. H. Dang, J. Hawecker,  E. Rongione, et al.

COLLECTIONS

 This paper was selected as Featured



View Online



Export Citation



CrossMark

ARTICLES YOU MAY BE INTERESTED IN

Spintronic terahertz emitter

Journal of Applied Physics **129**, 010901 (2021); <https://doi.org/10.1063/5.0037937>

Emergence of spin-orbit torques in 2D transition metal dichalcogenides: A status update

Applied Physics Reviews **7**, 041312 (2020); <https://doi.org/10.1063/5.0025318>

Perspective: Ultrafast magnetism and THz spintronics

Journal of Applied Physics **120**, 140901 (2016); <https://doi.org/10.1063/1.4958846>



Applied Physics
Reviews

Read. Cite. Publish. Repeat.

19.162

2020 IMPACT FACTOR*



Ultrafast spin-currents and charge conversion at 3d-5d interfaces probed by time-domain terahertz spectroscopy

Cite as: Appl. Phys. Rev. **7**, 041409 (2020); doi: [10.1063/5.0022369](https://doi.org/10.1063/5.0022369)

Submitted: 22 July 2020 · Accepted: 3 November 2020 ·

Published Online: 7 December 2020 · Corrected: 11 December 2020












View Online



Export Citation



CrossMark

T. H. Dang,¹ J. Hawecker,² E. Rongione,¹  G. Baez Flores,³ D. Q. To,¹ J. C. Rojas-Sanchez,¹  H. Nong,² J. Mangeney,² J. Tignon,²  F. Godel,¹  S. Collin,¹ P. Seneor,¹ M. Bibes,¹  A. Fert,¹ M. Anane,¹  J.-M. George,¹ L. Vila,⁴  M. Cosset-Cheneau,⁴ D. Dolfi,⁵ R. Lebrun,¹ P. Bortolotti,¹ K. Belashchenko,^{3,a)}  S. Dhillon,^{2,a)} and H. Jaffrès^{1,a)} 

AFFILIATIONS

¹Unité Mixte de Physique CNRS/Thales, University Paris-Sud and Université Paris-Saclay, 91767 Palaiseau, France

²Laboratoire de Physique de l'Ecole Normale Supérieure, ENS, Université PSL, CNRS, Sorbonne Université, Université de Paris, 75005 Paris, France

³Department of Physics and Astronomy and Nebraska Center for Materials and Nanoscience, University of Nebraska-Lincoln, Lincoln, Nebraska 68588, USA

⁴Université Grenoble Alpes, CEA, CNRS, Grenoble INP, Spintec, 38000 Grenoble, France

⁵Thales Research & Technology, 91767 Palaiseau, France

^{a)}Authors to whom correspondence should be addressed: belashchenko@unl.edu; Sukhdeep.Dhillon@phys.ens.fr; and henri.jaffres@cnrs-thales.fr

ABSTRACT

Spintronic structures are extensively investigated for their spin-orbit torque properties, required for magnetic commutation functionalities. Current progress in these materials is dependent on the interface engineering for the optimization of spin transmission. Here, we advance the analysis of ultrafast spin-charge conversion phenomena at ferromagnetic-transition metal interfaces due to their inverse spin-Hall effect properties. In particular, the intrinsic inverse spin-Hall effect of Pt-based systems and extrinsic inverse spin-Hall effect of Au:W and Au:Ta in NiFe/Au:(W,Ta) bilayers are investigated. The spin-charge conversion is probed by complementary techniques—ultrafast THz time-domain spectroscopy in the dynamic regime for THz pulse emission and ferromagnetic resonance spin-pumping measurements in the GHz regime in the steady state—to determine the role played by the material properties, resistivities, spin transmission at metallic interfaces, and spin-flip rates. These measurements show the correspondence between the THz time-domain spectroscopy and ferromagnetic spin-pumping for the different set of samples in term of the spin mixing conductance. The latter quantity is a critical parameter, determining the strength of the THz emission from spintronic interfaces. This is further supported by *ab initio* calculations, simulations, and analysis of the spin-diffusion and spin-relaxation of carriers within the multilayers in the time domain, permitting one to determine the main trends and the role of spin transmission at interfaces. This work illustrates that time-domain spectroscopy for spin-based THz emission is a powerful technique to probe spin-dynamics at active spintronic interfaces and to extract key material properties for spin-charge conversion.

Published under license by AIP Publishing. <https://doi.org/10.1063/5.0022369>

I. INTRODUCTION

The terahertz (THz) frequency range of the electromagnetic spectrum is generally defined as extending from 0.3 to 10 THz. It represents a spectral window that offers rich opportunities for advanced industrial applications in fields such as quality control, spectroscopy, imaging, medical diagnostics, security, telecommunications, and high-speed electronics. A range of promising THz sources techniques exist, as well new technologies that are being developed¹ along with

nondestructive testing, biodetection, cancer imaging, and microscopy using spintronics emitters.² A widespread method is based on THz time-domain spectroscopy (TDS) where THz pulses are typically generated from nonlinear optical crystals via optical rectification or from photoconductive switches with ultrafast transient currents when excited by an ultrashort near-infrared femtosecond oscillator.³ Nonetheless, the polar properties of the crystals and semiconductors used can strongly attenuate the THz radiation around optical phonon

resonances leading to strong spectral gaps in the emission. In this case, spintronic structures as novel THz sources may present real advantages in view of a broader THz emission window working at room temperature without spectral gaps.⁴ Indeed, since the pioneering experiments of Beurepaire *et al.* in 1996,⁵ followed by complementary investigations,^{6,7} it is now well established that the excitation of a magnetic material by an ultrafast laser pulse leads to a picosecond demagnetization of ferromagnetic films within the 3d band. Such a demagnetization process is accompanied by ultrafast hot carrier spin-currents in the 4-*sp* band, as proposed in MgO/Fe/Au multilayers.⁸ Recently, it has been demonstrated that spintronic elements composed of a ferromagnet (FM)/heavy metal (HM) bilayer can then emit relatively strong THz pulses owing to the conversion power of an excited spin-current into a transient dipole charges.^{4,9–12} From quantum mechanic rules, THz emitters also represent an alternative in the perspective to reach a high degree of linear polarization (>95%).

In the context of spintronics, ultrafast spin-to-charge conversion (SCC) is responsible for the emission of linearly-polarized THz electromagnetic dipolar radiation. SCC is made possible owing to the so-called spin-orbit interactions (SOI) near or at interfaces between a FM and an active material characterized by a large atomic number *Z* with strong SOI such 4*d* (Pd) or 5*d* (Pt, W, Ta, Au:Pt, Au:W, Au:Ta) HMs. Investigated extensively in the quasi-static excitation regime using ferromagnetic resonance (FMR) and spin-pumping (SP) techniques, SCC can occur via the inverse spin-Hall effect (ISHE)^{13–17} owing to an asymmetric deflection of the spin trajectory induced by SOIs. Moreover, SCC may also arise from the inverse Edelstein–Rashba effect (IREE) that occurs at spin-orbit split Rashba interfaces states.¹⁸ Such conversion was recently experimentally demonstrated on Rashba surface states^{19–21} and on surface states of topological insulators (TI) in the THz domain.²² Note that THz pulses from spintronic emitters only weakly depend on the circular polarization of the excitation laser beam, as observed from the optical selection rules in photogalvanic experiments.⁹ In contrast, the phase of the emitted THz radiation and E-field may be controlled with the magnetization direction^{21–23} and permitting specific E-field waveform emission.²⁴ This property is particularly appealing when considering an electrical control of the spin-based THz source output. Moreover, ultrafast SCC emitters possess the advantage of being phonon-less, resulting in the absence of any THz spectral dips, even at room temperature, and allowing extremely large unperturbed emission bandwidths (larger than 20 THz⁴) compared to other technologies based on femtosecond oscillators.

In an international context,^{4,9–12,25–32} HM and Rashba materials have shown large THz emissivity comparable to and even larger than that realized using mature nonlinear crystals such as ZnTe. Such emission properties are generally probed using a standard THz-TDS setup. The FM/HM junction, where Fe/Pt or Co/Pt represents the best candidates, exploits the ISHE with the so-called spin Hall angle (SHA), $\theta_{SHE} = j_c/j_s$. This represents the ratio between the transverse charge current j_c generated over the spin-current j_s source, as the main figure of merit of the local SCC. When summed over the active thickness of layers, SCC scales with a characteristic length ($\theta_{SHE} \times l_{sf}$), the product of the SHA with the spin-diffusion length l_{sf} (SDL), that lies around 0.2 nm for Co/Pt TMs. In the time-domain, this length matches the total volume of the transient dipole charge oscillations responsible for the dipolar emission. Improvements of the THz emission have been demonstrated using (1) engineered spintronic multilayers for optimal

energy absorption of the laser pulse³³ or (2) constructive interferences of ultrafast spin-currents in FMs with generated photoconductive carriers in a semiconductor switch,³² or using stacks of active multilayers.¹²

Beyond, the aforementioned spintronics structures are being extensively investigated for their spin-orbit torque (SOT) properties required for magnetic commutation functionalities. Progress in these materials is concentrated, in particular, on interface engineering for the optimization of the spin transmission.^{34–37,84} This is in order to significantly reduce the interfacial spin-loss as shown in recent experiments^{38,39} and more recently via first-principles calculations.^{40–44} The spin-transmission efficiency is generally determined by combining spin-pumping (SP) and SP-ISHE experiments in the ferromagnetic resonance (FMR) regime or alternatively by spin-transfer torque (STT-FMR) techniques revealing the SOT generated via reciprocal effects to spin-pumping. The process efficiency scales now with the electronic transmission, characterized as the spin-mixing conductance of the considered interface.^{39,45} The combination of SP-ISHE and THz techniques thus offers the ability to analyze the anatomy of spin-current injection in TM-based multilayers from which the electronic transmission appears to be the key physical parameter,^{38,39,46–48} as discussed very recently in the analysis of THz emission from spintronic emitters.^{49,50} Moreover, very recent experiments of SCC by FMR spin-pumping/ISHE methods foresee a possible breakthrough for THz emission supplied by Rashba-states exhibiting IEE characteristic lengths of 6 nm,⁵¹ thus largely exceeding the one of Co/Pt.

In this paper, using THz-TDS, we demonstrate and model a sizable spin-charge conversion and subsequent THz emission from transition metal (NiFe,Co)/Pt bilayers in the sub-picosecond timescale. The THz emission can be controlled by the direction of the magnetization in the plane of the FM layer revealing the ISHE origin. In particular, we extensively use the FMR spin-pumping/ISHE method to correlate the spin-injection temporal dynamics to the steady regime of spin-injection. We model such mechanisms by advanced *ab initio* methods and simplified finite difference time-domain simulations (FDTD). We show that, unlike similar 3*d*/5*d* NiFe/Au:W and NiFe/Au:Ta systems showing poor electronic transmission at interface, the strong benefit of Co/Pt lies in an optimized electronic transmission for the majority of spin-channel associated with a significant interfacial spin-asymmetry. By our numerical analysis method, we discuss the main issues giving rise to THz emission spectra and compare the main trends to more conventional spin-injection and spin-pumping experiments.

In particular, one aim of the paper is to point out the strong correlation between the THz emission power of a given system to the efficiency of spin-charge conversion obtained in radio frequency (rf) spin-pumping experiments. How does this correlation occur? The THz emission power (in units of the electric field E_{THz}) is proportional to an overall figure of merit $\eta \propto g^{\uparrow\downarrow} \times \sigma_{SHE} \times l_{sf}^{SOC}$ (in the case of ISHE process) displaying sequential electronic events and described by the product of the (1) the spin-mixing conductance (SMC) $g^{\uparrow\downarrow}$ connected to the interface electronic transmission, and as demonstrated by our numerical analyses by (2) the spin-Hall conductivity responsible for the spin-charge conversion, and by (3) the spin-diffusion length l_{sf} in the SOC material representing the volume of spin and charge relaxation. Note that in that picture, $g^{\uparrow\downarrow}$ represents the physical quantity probed also by FMR methods, except that the energy electron may

differ by some 100 meV. Importantly, *ab initio* calculations like presented in this contribution may answer that issue, also in order to optimize THz spintronic devices.

The main body of this paper is organized into four different sections. Section II is devoted to the description of the THz-TDS spectroscopy method, the different samples properties, and the resulting experimental data. Section III is devoted to the characterization of transition-metal-based systems by ferromagnetic resonance and spin-pumping-ISHE measurements in order to experimentally extract the electronic transmission at the relevant interfaces via ISHE and SCC processes. Section IV deals with *ab initio* electronic structure and electronic transmission coefficient calculations of Co/Pt and NiFe/Pt bilayers, linking the high THz emission efficiency to hot electron excitation, carrier diffusion, and spin-relaxation within spintronic bilayers and multilayers. Section V presents the results of the numerical simulations, analyses, and interpretations before addressing the main conclusions.

II. ULTRAFAST SPIN-CURRENTS AND SPIN-TO-CHARGE CONVERSION PROBED BY THz-TDS

THz emission from spintronic structures has been recently suggested to critically depend on the material properties like spin Hall angle and conductivity.⁴⁹ Here, we demonstrate how, for materials and active interfaces with equivalent properties, the interface qualities and electronic transmission are critical parameters for THz emission.⁵⁰ To this end, we specifically discuss and emphasize the experimental results of THz emission obtained on various spintronic Pt-,^{38,52,87} Au:W-,^{53,54} and Au:Ta⁵⁵-based samples investigated by THz-TDS. We compare such experiments, data, and analyses to complementary rf spin-pumping/ISHE results in the same series of samples (Sec. III). Indeed, the main intrinsic spin-Hall effect (SHE)/ISHE properties of these materials and interfaces have been previously largely investigated in the steady-state regime of spin injection by rf spin-pumping. They will be largely discussed now in terms of ultrafast spin-currents and subsequent conversion into transient charge current and THz emission. Co/Pt constitutes the actual reference in THz spintronic emitters. In particular, from an electronic point-of-view, we have previously

shown that Pt and Au:(W,Ta) materials differ in that their SHE/ISHE properties originate from the *intrinsic* nature of their spin-Hall conductivity in the case of Pt,^{15–17} while originating from the *extrinsic* side-jump effect for Au host-based alloys.⁵⁵ It results in an expected enhanced electronic scattering and a larger resistivity for disordered alloys that could give rise to an increase in the effective spin Hall angle, as also evidenced recently in the case of Pt.^{34–36,56,57} It may also be accompanied by an increase in the side-jump effect in the case of Au-based materials as discussed here. Moreover, we recall the general symmetry rules obeyed by the ISHE (SHE) phenomenon. ISHE can be described by a cross product of the three following vectorial quantities: the direction of the carrier spin σ , the direction of the spin-polarized carrier flow corresponding to the spin-current \mathbf{j}_s , and the outgoing charge current \mathbf{j}_c , according to the following relationship: $\mathbf{j}_c \propto \sigma \times \mathbf{j}_s$ ($\mathbf{j}_s \propto \sigma \times \mathbf{j}_c$ for SHE by Onsager reciprocal effects).

A. Principle and THz-TDS setup in the reflection mode

We briefly describe the experimental protocol and physical principles leading to the generation of the THz waves from spintronic emitters. Figure 1 shows sketches of the three major experiments we particularly focus on here: (1) the ultrafast spin-charge interconversion by ISHE after excitation by a short laser pulse, (2) the ultrafast spin-charge interconversion by IEE on Rashba states^{21,58} after excitation by a short laser pulse, and (3) the spin-pumping/ISHE via FMR methods. Regarding ISHE, we typically consider the Co/Pt structure as pictured in Fig. 1(a). Initially, the short laser pulse generates hot spin-polarized carriers by absorption, in particular, inside the ferromagnetic layer (Co), that diffuse to the Pt heavy metal (SOC material) after a short delay. ISHE may be considered as *bulk*-type in the sense that SCC occurs in the Pt layer at the interface with Co over a typical length scale given by the spin-diffusion length of the material (even shorter of the order of some nm). Penetrating into the heavy metal, the ultrafast spin-current $\mathbf{j}_s = \mathbf{j}_\uparrow - \mathbf{j}_\downarrow$ gives rise to an ultrafast transverse charge current, with a corresponding ratio $\mathbf{j}_c/\mathbf{j}_s$ given by the intrinsic SHA (θ_{SHE}). This effect is *bulk* also in the sense that the conversion is

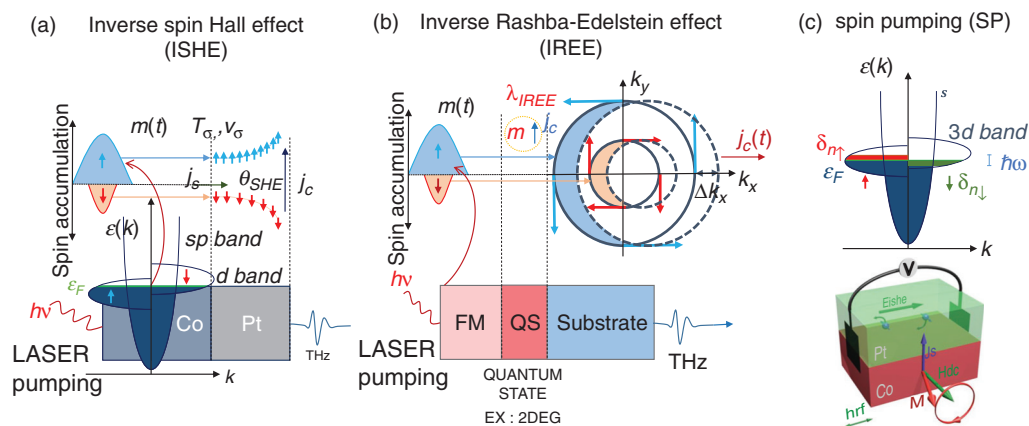


FIG. 1. Sketch representing the principles of operation of the three different experiments performed on spintronics interfaces that result in SCC through (a) laser-induced inverse spin-Hall effect (ISHE), (b) inverse Rashba-Edelstein effect (IREE), and (c) spin-pumping experiment. In the first two experiments, a short (100 fs) laser pulse excites hot spin-polarized electrons in the 4-*sp* conduction band diffusing out after some energy loss into the adjacent layer where SCC will occur (a) close to the interface by ISHE process or (b) via IREE process. (c) In the spin-pumping experiment, i.e., FMR-SP/ISHE, the out-of-equilibrium spin-density and spin-current are generated in the GHz regime in an energy range close to the Fermi level.

only possible from Bloch propagating electronic states. Although not the case for these bulk materials studied here, THz pulses can also be generated via IREE [Fig. 1(b)] at Rashba interfaces between ferromagnetic and two-dimensional materials or surface quantum states (e.g., topological insulators). IREE also results in SCC for THz generation, where a spin-accumulation at the Rashba interface generates an in-plane electric field transformed into a charge current,^{21,29,58} a phenomenon that we will not consider henceforth in this paper.

The THz-TDS experimental setup is shown in Fig. 2. The emitters were placed on a mount with a small magnetic field (between 10 mT and 0.2 T) parallel to the spin interface. An ultrafast (≈ 100 fs pulses) Ti:Sa oscillator centered at 810 nm was used to photo-excite the spin carriers directly from the front surface. Average powers of up to ≈ 600 mW were used with a repetition rate of 80 MHz. The typical laser spot size on the sample was about $200 \mu\text{m} \times 200 \mu\text{m}$. The generated THz pulses were also collected from the front surface of the spin-emitter (i.e., reflection geometry) using a set of parabolic mirrors of 150 and 75 mm focal length to focus on samples. Standard electro-optic sampling was used to detect the electric field of the THz pulses, using a 500- μm -thick (110) ZnTe crystal. A chopper was placed at the focal point between the second and third parabolic mirror to modulate the THz beam at 6 kHz for lock-in detection. A mechanical delay line was used to sample the THz ultrafast pulse as a function of time. The THz-TDS setup was placed in a dry-air purged chamber (typically $< 2\%$ humidity) to reduce water absorption of THz radiation.

B. Samples preparation and characterization: Main properties

The first set of samples are made of glass//Co(2)/Pt(4) and glass//NiFe(2)/Pt(4) 3d/5d transition-metal-based bilayers, where the

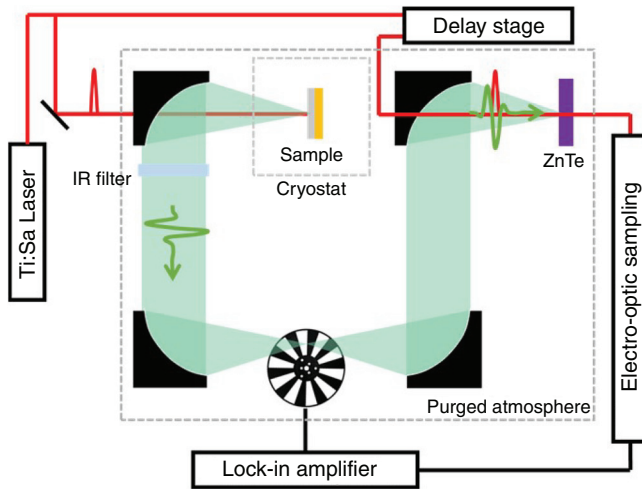


FIG. 2. Sketch of the THz-TDS experimental setup used in reflection mode to characterize spin-emitters. A standard Ti:Sa oscillator is used to generate 100-fs pulses with a repetition rate of 80 MHz centered at 800 nm. This beam is used to induce THz radiation in the spintronic emitter and to pump the non-linear crystal (ZnTe) for electro-optic sampling. The THz generated is mechanically chopped at 6 kHz to enable phase-sensitive detection or heterodyne detection (or lock-in detection). The time profile of the THz electric-field is then sampled by moving the delay line. More details are given in the text.

numbers in bracket indicate the thickness in nm. The structures are grown by magnetron sputtering in a single deposition chamber on borosilicate glass to avoid large backward THz absorption. The layer thickness was fixed after having calibrated the deposition speed on thicker films via x-ray reflectivity measurements. These samples constitute reference THz emitters characterized by emission power equivalent or larger than those obtained on ZnTe or GaP nonlinear crystals. A second series of 3d/5d transition metal samples are made of NiFe(2)/Au:W_{0.13}(4) and NiFe(2)/Au:Ta_{0.05}(4) structures deposited by co-sputtering (co-deposition) of the two pure materials. In (Co or NiFe)/Pt devices, Pt is known to provide an SHE mechanism that is scaled by an effective spin-Hall conductivity (σ_{SHE}^{Pt}) of $\sigma_{SHE}^{Pt} = 3.2 \times 10^3 \Omega^{-1} \cdot \text{cm}^{-1}$ ^{16,17} and a subsequent effective spin-Hall angle $\theta_{eff}^{Pt} = \rho_{xx} \sigma_{SHE}$ of about 0.05 in the in-plane current geometry (spin-current perpendicular to plane) owing to its resistivity of Pt, $\rho_{Pt} = 17 \mu\Omega \cdot \text{cm}$, at room temperature. Those physical parameters were determined via combined FMR-spin-pumping ISHE experiments on varying the Pt layer thickness.³⁸ On the other hand, Au:W^{53,54} as well as Au:Ta⁵⁵ impurity alloys are known to promote an extrinsic *side-jump* spin-Hall effect depending on the impurity content. The corresponding value may reach $\theta_{eff}^{Au:W} = 0.15$ for Au:W and $\theta_{eff}^{Au:Ta} = 0.4$ in the best alloys. The determination of those parameters was performed by using combined FMR-spin-pumping/ISHE measurements as well as possibly non-local spin-injection/detection in lateral spin-valve (LSV) devices when possible. The readers are invited to refer to Refs. 53 and 55 for details. In the present case, Au:W_{0.135} and Au:Ta_{0.05}, we get $\theta_{eff}^{Au:W} = 0.15$ and $\theta_{eff}^{Au:Ta} = 0.25$, respectively, corresponding to a spin-Hall angle larger than that of Pt. However, as expected, a much larger resistivity $\rho_{Au:W_{0.13}} = 90 \mu\Omega \cdot \text{cm}$ and $\rho_{Au:Ta_{0.05}} = 50 \mu\Omega \cdot \text{cm}$ compared to that of Pt $\rho_{Pt} = 17 \mu\Omega \cdot \text{cm}$ is measured at room temperature for those alloys. Material resistivity was measured via four-contacts van der Pauw method.

C. THz-TDS of ultrafast spin-currents

We describe the THz emission from the 3d/5d transition metal HM/FM elements as described above. Figure 3(a) displays the typical emitted electric field as a function of time for the Co/Pt sample at room temperature under a medium excitation power of 200 mW. Concerning the whole experiments, we have not observed particular strong heating of the different metallic samples mainly due to the fact the absorption of the laser power is limited to less than 20% for transition metal thin films. Moreover, experiments and THz signal show a strong reproducibility in time on the exact same sample series. Generally, THz signal highlights the relaxation in Pt of a hot electron spin-current, formed by spin \uparrow and spin \downarrow populations, that is converted to a transient charge current by ISHE. This displays the typical linear slope crossing the origin and representative of the derivative of the transient ultrafast charge current from SCC with $E_{THZ} \propto \frac{\partial I_c(t)}{\partial t}$ (like more detailed hereafter). The typical THz emission is comparable to that from a 0.5-mm-thick ZnTe crystal owing to optical rectification in the exact same experimental excitation conditions given in Sec. II A. [Similar THz pulses are obtained on Co/Pt samples grown on high-resistive (HR) Si substrates of about the same magnitude.] Figure 3(b) shows the typical experimental spectrum of the spintronic emitter obtained by Fourier transform of the temporal emission in the

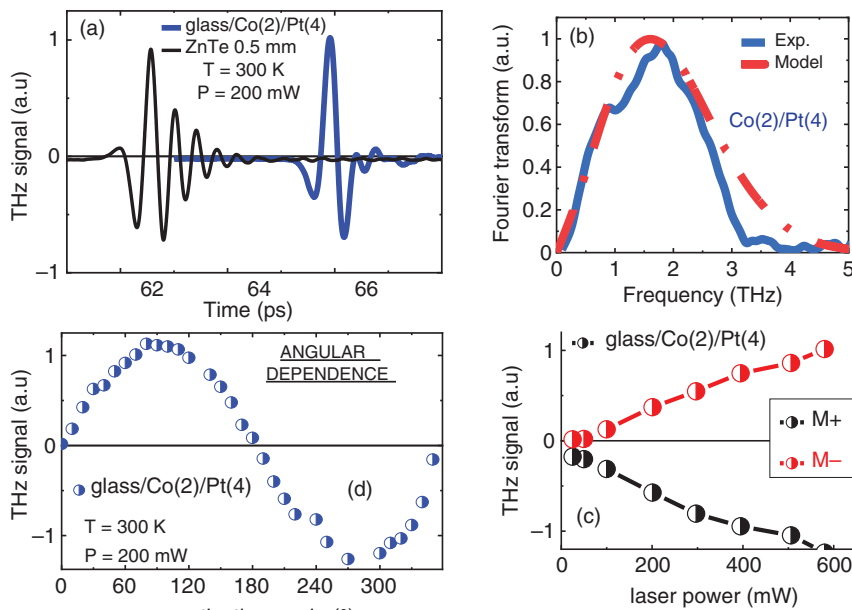


FIG. 3. (a) Temporal THz emission acquired using THz-TDS at room temperature on Co(2)/Pt(4) system under a 100-fs laser pulse with average power of $P=200$ mW. Comparison is shown with THz emission from ZnTe crystal via optical rectification under the same experimental conditions. (b) Experimental Fourier transform of the Co(2)/Pt(4) temporal signal giving the spectrum in the $[0 - 3]$ THz window (blue). Comparison with the modeling using parameters described in the text (red dashed line). (c) Amplitude of the maximum THz wave vs laser power excitation in the $[0 - 600]$ mW range, repetition rate of 80 MHz, and under two different opposite magnetic polarities. (d) Characteristic sine angular dependence of the THz-wave amplitude by varying the in-plane Co magnetization angle.

$[0 - 3]$ THz window, limited by our detection setup. From the literature,⁴ spintronic THz emitters are known to cover a wider emission range up to 30 THz.

Now, we anticipate the discussion about the modeling of such spectra, which will be discussed in more detail in Sec. IV, and give the main issues. In Fig. 3(b), the red dashed line displays the results of our modeling when one considers the spin-charge conversion into Pt in the time domain after an excitation pulse in Co. This has been derived from the spin-dependent Maxwell equation in a bilayer (FM/HM) taking into account high electronic transmission at interfaces (Sec. V) and high conductivity in the SOC material (Pt). We manage to reproduce conveniently the Fourier transform (FT) spectra by considering momentum τ and spin-relaxation time τ_{sf} for Co and Pt extracted from the literature for energy not too far from the Fermi energy (refer to Table I for physical parameters used). Indeed, the high electronic transmissivity at Co/Pt interface for a large energy window above the Fermi level makes less critical the energy-dependence of the carrier relaxation, and electron flow does not discard too much from a diffusive picture, before their fast relaxation in Pt. When the transmission is expected to vary much with energy and for a rather slow relaxation in the NM, e.g., a superdiffusive picture (not considered here) is necessary. Departing from this Co/Pt system, scaling up the relaxation rate of hot electrons, that is decreasing in proportion the momentum and spin relaxation time, is accompanied by an enhancement of the resistivity (case of NiFe/Au:W and NiFe/Au:Ta) and a loss of the THz signal due to a larger current dissipation. We give some modeling and simulation results in Sec. V.

Figure 3(c) demonstrates the variation of the electric field as a function of power and shows two important features. First, it demonstrates that the amplitude of the THz waveform increases almost linearly with the laser excitation power within the range $[0 - 600]$ mW. It will be shown to be very analog to the output transverse ISHE voltage vs rf-power in more conventional FMR-spin pumping-ISHE experiments. Second, the sign or polarity of the E-wave THz field can be

reversed upon magnetization reversal along two opposite directions. This is a particular feature of the THz emission from spin-current injection, and this originates from the direct quantum symmetry rules of the SHE/ISHE as discussed above. Indeed, Fig. 3(d) shows the typical angular dependence of the THz electric field when the applied magnetization is rotated in the film-plane over the full $[0 - 360]$ degrees range. We can observe an almost perfect sine angular variation where the angle $\theta_M = 0$ corresponds to the direction of the ZnTe crystal proper axis (direction of the analyzer). This exhibits a maximum of the signal when the magnetization is perpendicular to the detector principal axis or, equivalently, when the electric field is perpendicular to the magnetization direction according to the SHE/ISHE conversion rules.

Figure 4(a) displays the comparison of the THz-TDS spectra acquired between Co/Pt and NiFe/Pt samples at room temperature in the exact same excitation configuration. We observe an almost identical response in both cases, and this is in stark contrast to demagnetization experiments of the $3d$ magnetic band.⁵⁹ Our experiments show the equivalence of the two systems involving Co or NiFe as a ferromagnetic source when one considers, not the dynamics of the local $3d$ magnetization like in Ref. 59, but those of hot electrons in the $4sp$ bands location of mobile carriers. Moreover, one has performed equivalent experiments on glass//Co(2)/Al(2)/Al_{ox}(3) and glass//NiFe(2)/Al(2)/Al_{ox}(3) reference samples free of any heavy-metal layer. Results (not shown) display a signal for Co(2)/Al(2) on the order of 1/20 compared to Co(2)/Pt(4) and no observable signal for NiFe(2)/Al(2), giving thus the efficiency of self-emission (self-ISHE) for Co like reported recently.⁶⁰ One can conclude that the optimized performances obtained with $3d$ /Pt systems clearly identify Co/Pt and NiFe/Pt as one of the most relevant interfaces owing to their optimized spin-dependent electronic transmission. This will be shown theoretically by advanced *ab initio* methods in Sec. IV. We emphasize here the impact of two linked and key physical parameters for NiFe/Au:W and NiFe/Au:Ta systems on the THz emission, namely, (1) a larger spin Hall angle θ_{SHE} compared to Co/Pt reference (0.15 for

TABLE I. Material parameters used in the FDTD simulations.

Parameter	Use	Material	Value	Reference
Ferromagnetic layer thickness t_{FM}	Input	Co	2 nm	...
Lifetime of the majority spins τ_{\uparrow}	Input	Co	22 fs	77
Lifetime of the minority spins τ_{\downarrow}	Input	Co	7 fs	...
Velocity of the majority spins v_{\uparrow}	Input	Co	0.6 nm/fs	77
Velocity of the minority spins v_{\downarrow}	Input	Co	0.6 nm/fs	...
Diffusion of the majority spins D_{\uparrow}	$\frac{1}{3} \tau_{\uparrow} v_{\uparrow}^2$	Co	2.64 nm ² /fs	...
Diffusion of the minority spins D_{\downarrow}	$\frac{1}{3} \tau_{\downarrow} v_{\downarrow}^2$	Co	0.84 nm ² /fs	...
Spin asymmetry β	Input	Co	0.46	78
Mean free path λ	Input	Co	8.6 nm	79
Spin diffusion length l_{sf}	Input	Co	12 nm	78
Spin scattering time τ_{sf}	$\frac{6l_{sf}}{v_F \lambda (1-\beta)^2}$	Co	75 fs	...
Nonmagnetic layer thickness t_{NM}	Input	Pt	4 nm	...
Carrier lifetime $\tau = \tau_{\uparrow} = \tau_{\downarrow}$	Input	Pt	10 fs	80
Carrier velocity $v = v_{\uparrow} = v_{\downarrow}$	Input	Pt	0.35 nm/fs	80
Diffusion coefficient $D = D_{\uparrow} = D_{\downarrow}$	$\frac{1}{3} \tau v^2$	Pt	0.3 nm ² /fs	...
Mean free path λ	Input	Pt	3 nm	80
Spin diffusion length l_{sf}	Input	Pt	3 nm	38
Spin scattering time τ_{sf}	$\frac{6l_{sf}}{v_F \lambda}$	Pt	20 fs	81
Interfacial spin asymmetry γ	Variable	Co/Pt	+0.5	82
Interfacial spin resistance R_B	Input	Co/Pt	$0.83 \times 10^{-15} \Omega \bullet \text{m}^2$	82
Laser amplitude A	Input	...	1 a.u.	...
Laser pulse duration Δt	Input	...	100 fs	...
Interfacial transmission coefficient T^*	Variable	Co/Pt	$\{10^{-4} - 10^{-1}, 0.25, 0.5\}$...
Transmission of the majority channel T_{\uparrow}	Deduced	Co/Pt	see Eq. (16)	...
Transmission of the minority channel T_{\downarrow}	Deduced	Co/Pt	see Eq. (16)	...
Remagnetization time τ_r	Fixed	Co	10 ps	...
Spin-up channel source term s_{\uparrow}	Variable	Co	$\{0.5, 1\}$...
Spin-down channel source term s_{\downarrow}	Variable	Co	$\{0.5, 1\}$...

Au:W and 0.25 for Au:Ta), but also with (2) a larger alloying resistivity ρ due to scattering enhancement. Figure 4(b) (Au:W) and Fig. 4(c) (Au:Ta) display the typical THz emission for each case, showing the typical waveform of hot spin-current relaxation at the ps scale but with a strong reduction in field by a factor 20 compared to Co/Pt or NiFe/Pt. This observation is surprising as an increase by a factor between 2 and 5 would be expected owing to the larger SHA in the Au-based alloy systems. The results are summarized on Fig. 4(d). As demonstrated below, the reasons for such a decrease are potentially twofold: (1) the enhancement of the alloy resistivity strongly decreases the THz emission due to spin-current relaxation effects and (2) a reduction of the spin-transmission at NiFe/Au interfaces compared to Co/Pt or NiFe/Pt, as revealed by FMR-spin-pumping experiments.

III. SPIN-PUMPING EXPERIMENTS AND INTERFACE TRANSPARENCIES

The second type of experiment is FMR spin-pumping (FMR-SP) coupled to ISHE, which can be performed on the same type of structures.¹³ FMR-SP [Fig. 1(c)] consists of generating at the FMR

resonance, in the typical range 6–10 GHz, an out-of-equilibrium spin-current. SCC occurs as described above except that the out-of-equilibrium spin-polarized carriers remain within an energy range ϵ close to the Fermi energy ϵ_F ($\epsilon \simeq \epsilon_F \pm \hbar\omega$), leading to a small DC or voltage. This out-of-equilibrium spin-current is defined as

$$j_s^{\text{eff}} = \frac{2e^2}{\hbar} g_{\text{eff}}^{\uparrow\downarrow} \frac{\hbar\omega}{e} \sin^2(\theta_m) \propto P_{\text{rf}} \quad (1)$$

$$j_s^{\text{eff}} = \left(\frac{2e}{\hbar} \right) \frac{g_{\text{eff}}^{\uparrow\downarrow} \gamma^2 \hbar h_{\text{rf}}^2}{8\pi\alpha^2} \frac{4\pi\gamma M_{\text{eff}} + \sqrt{(4\pi\gamma M_{\text{eff}})^2 + 4\omega^2}}{(4\pi\gamma M_{\text{eff}})^2 + 4\omega^2},$$

where e is the electron charge; \hbar is the reduced Planck constant; $\omega = 2\pi f$ is the pulsation of the rf-field, with f the rf-frequency; $\gamma = g\mu_B/\hbar$ is the gyromagnetic ratio, with g the Landé factor and μ_B the Bohr magneton; M_{eff} is the effective saturation magnetization; and h_{rf} is the small oscillating rf transverse field responsible for precession. θ_m then stands for the average precessing angle of the magnetization around the local effective static field H_{DC} with the result that $\sin^2(\theta_m)$ is proportional to the rf-power absorbed by the ferromagnetic

material. It results that the charge current pumped after spin-charge interconversion in the heavy metal is directly proportional to $P_{rf} \propto \sin^2(\theta_m)$ and then to h_{rf}^2 ; and that a normalized value for it writes in A/G^2 .

The term *eff* corresponds to a *effective* renormalization compared to the maximum spin-current that can be injected and takes into account (1) the finite electron transparency at the interface and (2) a possible spin-backflow from the HM toward the FM. Note that in the previous expression, one has $\alpha = \alpha_0 + \Delta\alpha$, where α_0 is the bare damping free of spin-current dissipation and $\Delta\alpha$ is the damping enhancement due to spin-pumping. The expression of the spin-current injection by the α^2 factor in the denominator accounts for the reduction of the characteristic precession angle when α increases. Generally, the determination of the α parameter is performed by extracting the linear dependence and slope of the FMR linewidth vs the rf-frequency as performed previously in the case of the Co/Pt systems. $g_{eff}^{\uparrow\downarrow} = \sum_{k_{\parallel}} (1 - r_{\uparrow}^*)$ is the effective spin-mixing conductance per unit area of the corresponding interface, as a sum of both real and imaginary parts of the aforementioned quantity over the incoming k_{\parallel} channels. This non-zero quantity is thus responsible for the spin-current dissipation and FMR linewidth (α) enhancement with the result that the damping parameter α may vary over a very short length scale, smaller than 2 nm. Here, we give the main rules describing the spin-current dissipation at interfaces from spin pumping data. The increase

in the parameter α is generally related to $g_{eff}^{\uparrow\downarrow}$ by the following relationship:

$$\Delta\alpha = \frac{g_{\mu_B}^{\uparrow\downarrow}}{4\pi M_{eff} t_{FM}} g_{eff}^{\uparrow\downarrow}, \quad (2)$$

where t_{FM} is the thickness of the ferromagnetic layer. In this expression, $g_{eff}^{\uparrow\downarrow}$ is the effective spin-mixing conductance taking into account the spin-backflow process and spin-memory loss or SML.³⁸ The decrease in the spin-injection efficiency may reach 60% that way, and this loss of spin-injection efficiency can be treated by the so-called R_{SML} -coefficient^{38,41,44}

$$R_{SML} = \frac{j_s^{HM}}{j_s^{eff}} = \frac{r_{sI}}{r_{sI} \cosh(\delta) + r_{s,\infty}^{HM} \coth\left(\frac{t_{HM}}{l_{sf}^{HM}}\right) \sinh(\delta)} \quad (3)$$

where j_s^{eff} and j_s^{HM} are the spin-currents escaping the FM and the one injected in the HM, respectively, which may now differ. r_{sI} is the interfacial spin-resistance, ratio of the boundary resistance (interface resistance) r_b is the resistivity of the interface, and δ is the SML parameter. $r_{s,\infty}^{HM} = \rho_{HM} \times l_{sf}^{HM}$ is the spin-resistance of the heavy metal of thickness t_{HM} and spin-diffusion length l_{sf}^{HM} . R_{SML} appears as a *constant* in the sense that it does not depend on the spin-flip rate in FM. We have

$$g_{eff}^{\uparrow\downarrow} = g^{\uparrow\downarrow} \frac{r_{sI} \cosh(\delta) + r_s^{HM\infty} \coth\left(\frac{t_{HM}}{l_{sf}^{HM}}\right) \sinh(\delta)}{r_{sI} \left[1 + \frac{1}{2} \sqrt{\frac{3}{\varepsilon}} \coth\left(\frac{t_{HM}}{l_{sf}^{HM}}\right) \right] \cosh(\delta) + \left[r_s^{HM\infty} \coth\left(\frac{t_{HM}}{l_{sf}^{HM}}\right) + \frac{1}{2} \frac{r_{sI}^2}{r_s^{HM\infty}} \sqrt{\frac{3}{\varepsilon}} \right] \sinh(\delta)}, \quad (4)$$

where $\varepsilon = \tau_p/\tau_{sf}^{HM}$ is the spin-orbit parameter (probability of spin-flip after diffusion). Typically, $\varepsilon \simeq 0.1$ for Pt with an even larger value for Au:W and Au:Ta transition-metal alloys. SML and effective SMC, like discussed above, are very important issues in the field of spin-orbit torques, and THz emission spectroscopy may represent a powerful method in the future to probe the exact anatomy of spin-current at spintronic interfaces like displayed in a recent literature.

A. Samples preparation and FMR spin-pumping setup

We now turn to experimental data acquired on Pt^{38,61} and Au-based alloys materials.^{53–55} For these experiments, we prepared a series of thicker ferromagnetic and spin-orbit-based material samples, respectively, Co(15)/Pt(30), NiFe(15)/Pt(30), as well as NiFe(15)/Au:W_{0.135}(30) and NiFe(15)/Au:Ta_{0.05}(30) grown by magnetron sputtering in a single deposition chamber on SiO₂-terminated Si wafers and in the exact same conditions as the ones prepared on glass for the THz emission experiments. A thicker ferromagnetic layer (15 nm) is suitable to enhance to the FMR resonance, whereas the thicker SOC material is beneficial to avoid the electrical rectification contribution to

the signal. Indeed, in spin-pumping experiments, the generation of a charge current into Pt needs to avoid a too lateral expansion in the ferromagnet where anisotropic magnetoresistance (AMR) and planar Hall effect (PHE) may give rise to a spurious electrical signal of a well-defined angular dependence.⁶² Samples were then cut in an elongated rectangular shape of typical dimension $L \times W = 2.5 \times 0.5$ mm². Combined FMR and inverse spin-Hall effect (ISHE) measurements were performed at room temperature in a split-cylinder microwave resonant cavity. The rf magnetic field h_{rf} was set along the long axis, and the external applied DC magnetic field H_{dc} was set along the width of the rectangle. The frequency of h_{rf} was fixed around $f = 9.6 - 9.8$ GHz, whereas H_{dc} was swept through the FMR resonance condition. The strength of h_{rf} was determined by measuring the quality factor (Q) of the resonant cavity with the sample placed inside for each measurement. At the resonance condition, the derivative of FMR energy loss was acquired as the voltage was recorded across the long extremity of the sample, that is, along the perpendicular direction to the H_{dc} field and magnetization. We have also performed frequency dependence within the 3 – 24 GHz range of the FMR spectrum in order to extract the effective saturation magnetization M_{eff} as well as

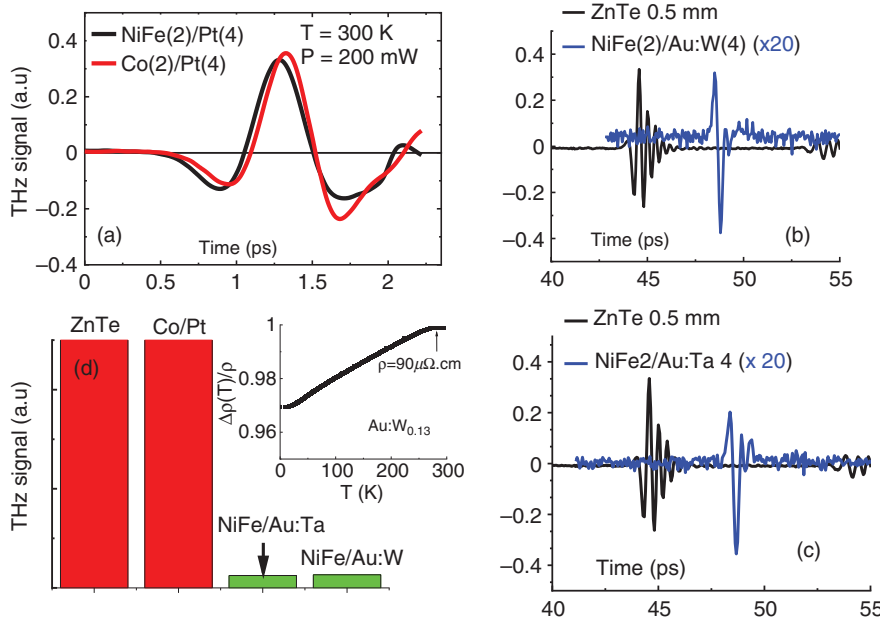


FIG. 4. (a) Comparison of the THz emission at room temperature ($P = 200$ mW) acquired on Co(2)/Pt(4) and NiFe(2)/Pt(4) samples showing similar features and equivalent amplitudes. (b) and (c) Emission of NiFe/Au:(W,Ta) systems compared with ZnTe(110) crystal. Measurements taken at room temperature under a laser fluence of $P = 200$ mW. (d) Peak-to-peak amplitude comparison between the well-known THz emitter ZnTe(110) and spintronic-based emitters including the reference Co/Pt and NiFe/Au:(W,Ta) systems. Inset of (d) Temperature variation of the resistivity $\frac{\Delta\rho_{Au:W_{0.13}}}{\rho}$ of Au:W_{0.13} from 300 to 10 K showing a small decrease in 3%. The sample Au:W_{0.13} corresponds to a typical resistivity of $\rho \simeq 90 \mu\Omega \cdot \text{cm}$ at RT for an approximate W content of about 13%.

the damping constant α . A refined analysis of the damping constant generally requires a reference sample free of spin-current dissipation at interfaces, i.e., without spin-memory loss (SML). Ideally, one would use a single Co layer capped by an oxidized Al capping layer.

B. Experimental results

We first focus on the results obtained on Co/Pt and NiFe/Pt characterized by a high electronic transparency and large THz emission. Figures 5(a) and 5(c) display the typical FMR spectra in the neighborhood of the resonance at frequency $f = 9.8$ GHz by sweeping the dc in-plane magnetic field. These typical spectra, corresponding to the field derivative of the FMR absorption $\frac{d\mu''}{dH_{dc}}$, are almost unchanged when the magnetization is reversed (dc field) $+M \rightarrow -M$ in the cavity and are almost equivalent for the two samples made of Co or NiFe (Py). Figures 5(b) and 5(d) display, in each case, the corresponding field dependence of the resulting transverse ISHE current I_C . This ISHE current level has been extracted by dividing the acquired transverse voltage by the device resistance ranging between 30 and 90 Ω . In both cases of Co and NiFe-based samples, the level of current lies in the range $0.6 - 0.7 \mu\text{A} \cdot \text{G}^{-2}$, which is a signature of a very high carrier transmission efficiency and an efficient spin-charge interconversion for Pt with spin-Hall angle close to $\theta_{eff}^{Pt} \simeq 0.05$. The spin-Hall angle for Pt can be largely enhanced by current in-plane configuration (CIP), alloying with a transition-metal species or synthesized in multilayered stacks.^{39,46} Moreover, when the dc external field and consequently the magnetization are reversed by 180°, the sign of the ISHE current I_C changes polarity, as is expected by the SCC rule from the ISHE $\mathbf{j}_c \propto \mathbf{j}_s \times \hat{z}$, where \hat{z} is the carrier flow direction. From Eq. (4), this results in the spin-mixing conductance at saturation for Co/Pt to be estimated as $g_0^{\uparrow\downarrow} \simeq 80 \times 10^{18} \text{ m}^{-2}$, giving rise to an effective spin-mixing conductance $g_{eff}^{\uparrow\downarrow} = \frac{g_0^{\uparrow\downarrow}}{1+g_0^{\uparrow\downarrow} r_{sj}} \simeq 22 \times 10^{18} \text{ m}^{-2}$ mainly limited by

the SML resistance r_{sj} . A similar value of $g_{eff}^{\uparrow\downarrow}$ for NiFe/Pt is found, in agreement with the work of Berger *et al.*³⁹

We now turn to the NiFe/Au:W and NiFe/Au:Ta sample series, displayed respectively in Figs. 6 and 7 and characterized by a high spin-conversion efficiency (larger SHA) but modest THz emissivity. In these samples, the resistivity for Au:W and Au:Ta, $\rho \simeq \frac{\hbar}{e^2} \left(\frac{2\pi}{k_F}\right)^2 N_D \sigma_{sc}$, measured by four-points van per Pauw method (N_D is the impurity content, k_F is the Fermi wavevector, σ_{sc} is the scattering cross section, and $\lambda_{mfp} = N_D^{-1} \sigma_{sc}^{-1}$ is the mean free part insensitive to the temperature), is expected to be almost insensitive to phonon scattering and then to temperature due to the dominant role of impurities like measured previously on Au:W_{0.07}, where $\frac{\Delta\rho}{\rho} \simeq 3\%$ from 300 K to 10 K [see Fig. 4(d) inset for the case of Au:W_{0.13}].⁵³ From the previous expression it is possible to extract a rough value of the scattering cross section of W impurities in Au in the case of Au:W. If one considers average Fermi wavevector in Au of the order of $k_F = \frac{\pi}{2a}$, where a is the lattice parameters, one obtains a pretty short distance $\frac{\sigma_{sc}}{a} \simeq 1.5 \text{ \AA}$, thus corresponding to a strong impurity screening by the noble Au metal as a host. That way, we also expect $I_{sf}^{Au:(W,Ta)}$ to be independent of the temperature for the same reasons that the phonon bath plays only a minor role in the electronic diffusion.

The resonance frequency f vs the magnetic field H_{res} [the derivative resonance spectra acquired for $H_{DC} \approx 100$ mT are reported on Figs. 6(a) and 7(a) for W- and Ta-based alloys] allows us to extract the effective magnetic saturation and the in-plane anisotropy in each case. We could observe that the NiFe layer possesses the same effective magnetization compared to the reference Py sample of about $760 \text{ emu} \cdot \text{cm}^{-3}$ and a negligible in-plane magnetic anisotropy (H_{uni}). Furthermore, the contribution due to inhomogeneities is very small, < 0.1 mT, and a small but clear increase in the damping constant for Au:W (4 nm) can be observed with respect to the reference sample. Thus, we can conclude that the Au:W layer acts as a spin sink layer.

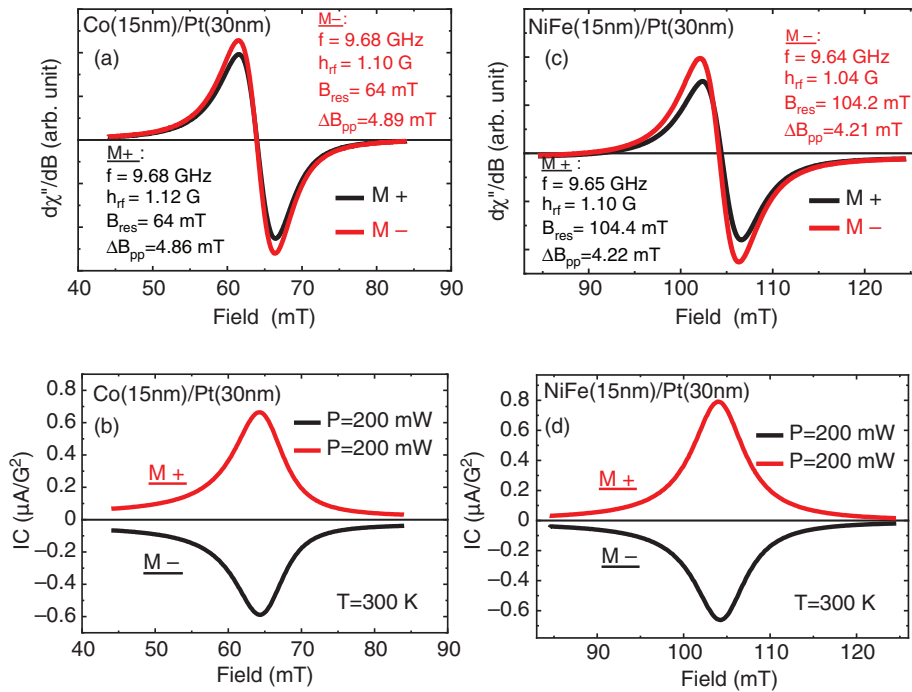


FIG. 5. Ferromagnetic resonance (FMR) acquired by the derivative of the absorption spectra for the respective positive ($M+$) and negative ($M-$) magnetization directions for (a) Co(15)/Pt(30) and (c) NiFe(15)/Pt(30) samples. The frequency is fixed at $f = 9.68$ GHz and the rf-field is about $h_{rf} = 1.1$ G. (b) and (d) Corresponding ISHE current spectra acquired on Co(15)/Pt(30) and NiFe(15)/Pt(30), respectively, in the same experimental conditions and displaying the same quantitative and qualitative output signal.

This can be verified in the charge current via constant V_C measurements from which we have extracted I_C where we may observe a symmetrical Lorentzian current peak at the resonance field [Figs. 6(b) and 7(b)]. Such Lorentzian dc peak for the current is linearly dependent on the rf-power injected in the cavity. To quantify the spin-Hall angle of this material, we used all our experimental values taking advantage of the spin diffusion length already determined, and the results are reported elsewhere.^{53–55} The bare damping constant for Py was found to be $\alpha_{NiFe} = (6.9 \pm 0.1) \times 10^{-3}$ originating from inhomogeneous broadening. This allows us to estimate the effective spin-mixing conductance g_{eff} for Au:W and Au:Ta and thus the spin-current density j_s injected by SP-FMR. The effective spin mixing conductivity is then extracted to be smaller than the Co/Pt and NiFe/Pt, that is, $g_{eff}^{\uparrow\downarrow} \simeq 6 \times 10^{18} \text{ m}^{-2}$ for Au:W and $g_{eff}^{\uparrow\downarrow} \simeq 4 \times 10^{18} \text{ m}^{-2}$ for Au:Ta. A typical factor of 5 in the electronic transmission then differs between Co/Pt or NiFe/Pt and NiFe/Au based alloys in favor of Co/Pt.

However, one must note that in spin-pumping experiments, a smaller value of $g_{eff}^{\uparrow\downarrow}$ does not necessarily imply a much smaller value of the spin-current injected, owing to the larger precession angle of the magnetization for smaller spin-current dissipation at low electronic transparency. In the present case, a slightly larger spin-Hall charge current I_C extracted at resonance compared to Co/Pt or NiFe/Pt systems can be understood as a result of a larger spin-Hall angle and larger precession angle despite an effective spin-mixing conductance reduced by more than a factor of 3. However, one can anticipate that the THz emission properties are very dependent on the local resistivity ρ of the material, a larger resistivity being detrimental for the observation of an efficient THz signal.

IV. MODELING OF THE THz-TDS SPECTRA

The specific exciting pulse laser mode requires some additional comment about modeling. Actually, two model pictures are admissible

based on different physical pictures: (1) a modeling of electron dynamics in the sub-picosecond scale, by which the local heating leads to transient precessing of electrons around a local change of the anisotropy magnetic field;^{63,64} this constitutes a direct extension to the GHz precession regime, which we do not consider henceforth in this section; or (2) a two temperature model by which an electronic absorption gives rise to electronic heating with characteristic excitation energy over the Fermi level (temperature T_e followed by inelastic relaxation due to electron-electron interactions and phonon bath characterized by a second temperature T_{ph}).⁶⁵ A refined modeling generally requires a *superdiffusive modeling* for excited carriers that we can further consider. Note that in this scenario, the fast energy and spin relaxation rate in the SOC transition metals (Pt, Au:W, Au:Ta) make that the two different temperature dynamics become more and more uncoupled leading to the sole electron dynamics relevant in the THz emission spectra.

The modeling presented in this section addresses (1) the time-dependent diffusion and relaxation processes in separate layers of excited spin-polarized carriers, generated by a short laser pulse and characterized by a certain generation rate $\mathcal{P}(\mathbf{r}, t)$; (2) the reflection/transmission of the spin-polarized hot carriers at the inner interface; as well as (3) the specific boundary conditions to consider at the two outward interfaces. With regard to point (2), the transmission across the inner interface can involve spin-mixing terms related to spin-flips and spin memory loss like exhibited in FMR spin-pumping experiments.

A. Boltzmann formalism

The description of the time-domain dynamics of the hot-electrons within spintronic multilayers excited by ultrashort laser pulses may be performed in the frame of the Boltzmann transport theory and equations (BTE), and considering the different electronic

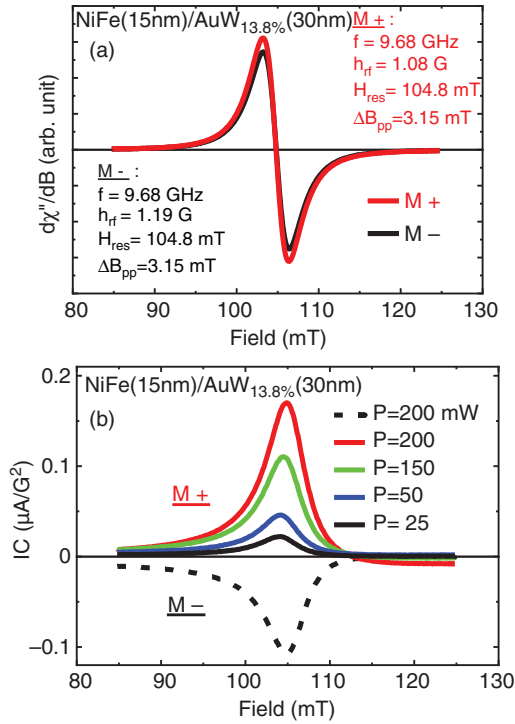


FIG. 6. (a) Ferromagnetic resonance (FMR) acquired at room temperature by the derivative of the absorption spectra for positive ($M+$) and negative ($M-$) magnetization directions for NiFe(15)/Au:W_{0.135}(30). The frequency is fixed at $f = 9.68$ GHz and the rf-field is about $B_{rf} = 1.1$ G. The resonance field was found to be 104.8 mT in each case. This emphasizes the same absorption spectra acquired when switching the direction of magnetization. (b) Inverse spin-Hall effect (ISHE) current spectra acquired corresponding to the exact same experimental conditions and for different rf-power (from 20 mW to 200 mW). The sign inversion of the DC-current signal is representative of the ISHE effect. Note that the ISHE signal increases almost linearly with the rf-power injected.

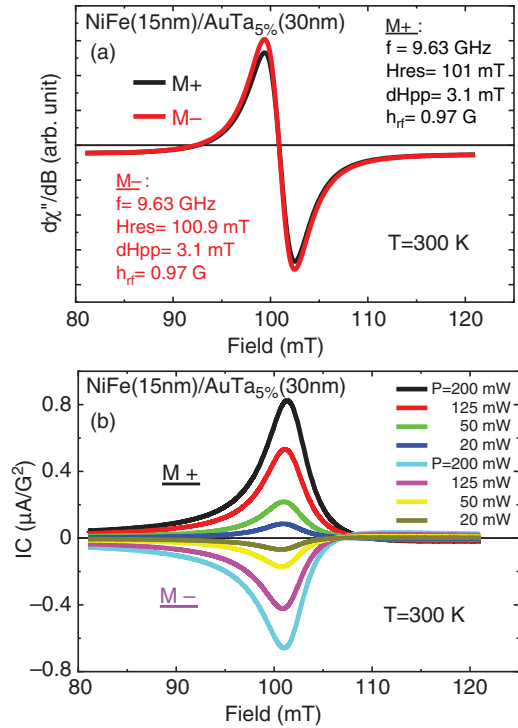


FIG. 7. (a) Ferromagnetic resonance (FMR) acquired at room temperature by the derivative of the absorption spectra for positive ($M+$) and negative ($M-$) magnetization directions for NiFe(15)/Au:Ta_{0.05}(30). The frequency is fixed at $f = 9.68$ GHz and the rf-field is about $B_{rf} = 1$ G. The resonance field was found to be 101 mT in each case. This emphasizes the same absorption spectra acquired when switching the direction of magnetization. (b) Inverse spin-Hall effect (ISHE) current spectra acquired corresponding to the exact same experimental conditions and for different rf-power (from 20 mW to 200 mW). The sign inversion of the DC-current signal is representative of the ISHE effect. Note that the ISHE signal increases almost linearly with the rf-power injected.

diffusion and relaxation processes. The BTE for spin-polarized particles can be derived as the evolution equation of a reduced single-particle density matrix. It also accounts for the properties of excited electron dynamics in the sp bands of very thin metal layers, as widely discussed in the superdiffusive theory of spin-currents in both experiments and in modeling.^{50,65–67} We start from the evolution equation for the carrier-distribution function in the following form:

$$\left[\frac{\partial}{\partial t} + \frac{\hbar}{m^*} \mathbf{k} \cdot \nabla_{\mathbf{r}} + \frac{1}{\hbar} \mathbf{E}_{\sigma}(\mathbf{r}, t) \cdot \nabla_{\mathbf{k}} \right] f_{\sigma}(\mathbf{r}, \mathbf{k}, t) = \mathcal{P}_{\sigma}(\mathbf{r}, \mathbf{k}, t) - \frac{f_{\sigma}(\mathbf{r}, \mathbf{k}, t)}{\tau_{\sigma}(\mathbf{r}, E)} + \sum_{\sigma', \mathbf{k}'} \int d^3 k' w(\mathbf{r}; \mathbf{k}', \sigma'; \mathbf{k}) f_{\sigma'}(\mathbf{r}, \mathbf{k}', t), \quad (5)$$

where f_{σ} represents the spin- and time-dependent distribution function in space (\mathbf{r}) and in the reciprocal space or Brillouin zone (\mathbf{k}), \mathbf{E} is the electric field, and $\mathcal{P}_{\sigma}(\mathbf{r}, \mathbf{k}, t)$ is the pump term due to the pulsed laser excitation. In general, the distribution function $f_{\sigma} = f_{\sigma}^0 + \phi_{\sigma}$ can be separated into a sum of an equilibrium part $f_{\sigma}^0(E)$ plus a non-equilibrium (thermal) part $\phi_{\sigma}(\mathbf{r}, \mathbf{k}, t)$,⁶⁸ describing thus the electronic excitations (ϕ_{σ} is called g_{σ} in Ref. 68). The two relaxation terms at the

right-hand side of Eq. (5) represent the respective *scattering-out* and *scattering-in* processes in the BTE.

We denote the FM layer as the left material (L), while the right one (R) is the heavy metal characterized by a strong SOI, the location of strong spin-relaxation processes. We focus here on a Co/Pt system giving convincing qualitative and quantitative results when compared to the experiments. The ensemble of the physical parameters used is listed in Table I. The dynamics of the system is performed using the so-called wave-diffusion modeling as described in Refs. 49, 69, and 70, involving the time dynamics of both spin-dependent carrier densities [Eq. (6)] and spin-currents [Eq. (6)]. We have included relevant relaxation terms⁶⁹ and potentially may include local secondary electron sources that we do not consider henceforth. The wave-diffusion model leads to complex differential equations to solve in space, and we time considering the same kernel for both spin densities and currents, but admitting a different source term. The reader can refer to Appendix B for more details on the differential equation.

Equation (6) is called the population evolution as it is made of three parts: a spin-flip term associated with inelastic spin-flip scatterings, the current divergence, and the spin-dependent source term

(laser). This absorption gives rise to excitation of electrons from the d band to unoccupied states from the sp bands above the Fermi level with energy of the order of a fraction of an eV. Besides, Eq. (6) describes the spin-current dynamics dependent on the momentum relaxation time τ_{sf}^i . Moreover, we may include re-magnetization process at a larger timescale τ_r by adding a supplementary $sp \rightarrow d$ relaxation term. We thus consider the two-coupled equations in the time-domain, valid for both layers $i = \{L, R\}$, according to

$$\frac{\partial n_{\sigma}^i}{\partial t} = - \underbrace{\frac{n_{\sigma}^i - n_{\sigma}^i}{\tau_{sf}^i}}_{\text{spin-flip}} - \underbrace{\nabla j_{\sigma}^i}_{\text{flux term}} + \left(\underbrace{\mathcal{P}_{\sigma}(\mathbf{r}, t)}_{\text{source term}} - \underbrace{\frac{n_{\sigma}^i}{\tau_r^i}}_{\text{remag}} \right) \delta_{i,L} \quad (6)$$

$$\frac{\partial j_{\sigma}^i}{\partial t} = - \frac{j_{\sigma}^i}{\tau_{sf}^i} - \frac{D_{\sigma}^i}{\tau_{sf}^i} \nabla n_{\sigma}^i,$$

which has to be fulfilled. $\sigma = \{\uparrow, \downarrow\}$ represents the spin channel with $\bar{\sigma} = -\sigma$, $n_{\sigma} = n_{\sigma}(\mathbf{r}, t)$ the population density for each spin channel and $j_{\sigma} = j_{\sigma}(\mathbf{r}, t)$ the current density for each spin channel. $D_{\sigma} = \frac{1}{3} v_F^2 \tau_{sf}$ is the spin-dependent diffusion coefficient in the corresponding material with v_F , the characteristic Fermi velocity of the sp band. τ_{sf} is the spin scattering time and $\mathcal{P}_{\sigma}(\mathbf{r}, t) = \mathcal{P}_{\sigma}(t)$ the spin-dependent source term that we assume to be homogeneous over the whole ferromagnetic layer thickness.

In the limit $t < \tau_r$, these coupled equations lead to the determination of both out of equilibrium magnetization (the so-called *spin-accumulation*) $m = n_{\uparrow} - n_{\downarrow}$ and spin-current $j_s = j_{\uparrow} - j_{\downarrow}$ via the following second-order differential equations:

$$\frac{\partial^2 m}{\partial t^2} + \left[\frac{1}{\tau} + \frac{1}{\tau_{sf}} \right] \frac{\partial m}{\partial t} + \frac{m}{\tau \tau_{sf}} - \frac{\tilde{D}}{\tau} \frac{\partial^2 m}{\partial z^2} = \frac{\partial \mathcal{P}}{\partial t} \quad (7)$$

$$\frac{\partial^2 j_s}{\partial t^2} + \left[\frac{1}{\tau} + \frac{1}{\tau_{sf}} \right] \frac{\partial j_s}{\partial t} + \frac{j_s}{\tau \tau_{sf}} - \frac{\tilde{D}}{\tau} \frac{\partial^2 j_s}{\partial z^2} = - \frac{\tilde{D}}{\tau} \frac{\partial \mathcal{P}}{\partial z} \quad (8)$$

for large τ_r , $\tilde{D} = \frac{2D_{\uparrow}D_{\downarrow}}{D_{\uparrow}+D_{\downarrow}}$ is the average diffusion constant, $\tilde{\tau} = \frac{2\tau_{\uparrow}\tau_{\downarrow}}{\tau_{\uparrow}+\tau_{\downarrow}}$ the average scattering time, and $\mathcal{P}(t) = \mathcal{P}_{\uparrow} - \mathcal{P}_{\downarrow}$ the time-profile of the spin-polarized pump.⁸⁶ Note that for a steady-state regime whereby all quantities no longer depend on time, one obtains the standard space-dependent exponential variation $m, j_s \propto \exp\left(\pm \frac{z}{l_{sf}}\right)$ with an exponential decay given by the spin diffusion length, related to the spin-lifetime and diffusion coefficient \tilde{D} according to $l_{sf} = \sqrt{\tilde{D}\tau_{sf}}$.

The far-field THz electric field E_{THz} emitted is proportional to the time derivative of the local charge current j_{σ} , and it is derived from the following expression:

$$E_{THz} \propto \frac{\partial \int j_{\sigma} dz}{\partial t} = -\theta_{SHE} \int \left(\frac{j_s}{\tau} + \frac{\tilde{D}}{\tau} \frac{\partial m(z, t)}{\partial z} \right) dz \quad (9)$$

with the charge current $j_{\sigma}^{3D} \simeq \theta_{SHE} j_s$ proportional to the spin-current for ISHE and $\int dz$ means that one operates the integral over the thickness of the HM layer corresponding to a summation over all the emitting dipole. On the other hand, by operating a Fourier transform (FT) on Eq. (6) acting respectively on $m(z, t) = n_{\uparrow}(z, t) - n_{\downarrow}(z, t) = \int \tilde{m}(q, \omega) \exp[i(qz - \omega t)] dq d\omega$ and $j_s(z, t) = j_{\uparrow}(z, t) - j_{\downarrow}(z, t) = \int \tilde{j}_s(q, \omega) \exp[i(qz - \omega t)] dq d\omega$, one may derive

$$\tilde{m}(z=0, \omega) \simeq \frac{\kappa \tau_{sf}}{1 - i\omega \tau_{sf}} \tilde{j}_s(z=0, \omega), \quad (10)$$

$$\tilde{j}_s(z=0, \omega) = - \frac{D}{1 - i\omega \tau} \nabla_z \tilde{m}(z=0, \omega), \quad (11)$$

where $\kappa^{-1} = (iq)^{-1} \simeq l_{sf} = \sqrt{D\tau_{sf}}$ is the typical spin diffusion length over which dipoles are active. From Eq. (11), and by expressing the longitudinal conductivity $\sigma = \sigma_{xx} = e^2 D \mathcal{N}$ (\mathcal{N} is the density of states), one may thus derive

$$E_{THz} \propto \frac{i\theta_{SHE}\omega\tau_{sf}D\kappa}{(1 - i\omega\tau)(1 - i\omega\tau_{sf})} \tilde{j}_s(z=0, \omega) \quad (12)$$

$$E_{THz} \simeq \frac{i\omega\tau_{sf}\kappa}{(1 - i\omega\tau)(1 - i\omega\tau_{sf})} \left(\frac{\sigma_{SHE}}{\mathcal{N}(E)e^2} \right) \tilde{j}(\omega, z=0).$$

Note that for HM materials like Pt, one has $\tau_{sf} \gtrsim \tau$. From Eq. (12), it results that, at equivalent amplitude for the source term \tilde{m} , the time-domain charge current and subsequent electric field are proportional to the diffusion constant and then to the conductivity of the HM layers. In particular, Eq. (12) proves that, unlike the spin-orbit torque (SOT), no real enhancement of the THz signal is expected if the *intrinsic* spin-Hall conductivity σ_{SHE} of intrinsic SHE materials, like Pt or Au, is kept fixed or even decreases by alloying despite a possible increase in the effective spin-Hall angle θ_{SHE} . This partly explains that poorly conductive materials or alloys like Au:W or Au:Ta provide only modest THz emission compared to Co/Pt or NiFe/Pt.

B. *Ab initio* calculations of transparencies at Co/Pt interfaces

First-principles calculations giving the energy-dependence of the electronic transmission coefficient for the Co/Pt(111) interface were performed within the atomic sphere approximation in the Green's function-based tight-binding linear muffin-tin orbital (GF-LMTO) method,⁷¹⁻⁷³ treating exchange and correlation within the local-density approximation (LDA).^{74,85} The Green's functions are represented in a mixed basis: the two-dimensional translational periodicity of the interface allows one to introduce the conserved wave vector component \mathbf{k}_{\parallel} parallel to the interface, which is confined to the two-dimensional Brillouin zone of the interface; the Green's function is then a matrix in real space with arguments confined to the unit cell of the "active region" including the interface and a few monolayers on each side of it. The active region is embedded between semi-infinite Co and Pt leads. After the self-consistent charge and spin densities were obtained, the total and \mathbf{k}_{\parallel} -resolved energy-dependent ballistic conductance of the Co/Pt bilayer was calculated using the Landauer-Büttiker technique.

We assumed the Co/Pt bilayer has a perfect continuous face-centered cubic lattice with an abrupt (111) interface and a common lattice parameter of 2.64 Å, ignoring strain relaxation. The average transmission probability for electrons incident from the Co side is

$$\bar{T}_{\sigma}^{\text{Co} \rightarrow \text{Pt}} = \frac{1}{N_{\sigma}^{\text{Co}}} \sum_n T_{\sigma}^n = \frac{g_{\sigma}}{g_{\sigma}^{\text{Co}}} \quad (13)$$

where σ denotes the spin channel, N_{σ}^{Co} is the number of conducting channels of a given spin in the Co lead, T_{σ}^n is the transmission probability for one of these channels n , g_{σ} is the conductance of the Co/Pt

bilayer, and g_{σ}^{Co} is the Sharvin conductance of the Co lead. The \mathbf{k}_{\parallel} -resolved transmission function for the Co/Pt (111) interface is shown in Fig. 8, for each spin channel, at 0, 0.5, and 1.0 eV above the Fermi level. One of a relevant quantity for the electronic transport property is the average transmission probability [Eq. (13)] for each spin channel as shown in Fig. 9(a). The origin of the features observed in these plots can be correlated with the density of states (DOS) of bulk Co and Pt, as discussed below.

Cobalt has one majority-spin Fermi-surface sheet with topology identical to that of Cu: the somewhat distorted free-electron-like Fermi surface does not quite fit into the first Brillouin zone, forming “necks” centered around the L points on its hexagonal faces. One of these L points projects onto the center (Γ point) of the surface Brillouin zone of the (111) interface, resulting in a circular “hole” in the transmission function [Figs. 8(a)–8(c)] where there are no bulk states in Co. As the energy increases, the iso-energetic surface expands, and the holes become larger. Figures 8(a)–8(c) show that most of the states from the majority-spin Fermi surface sheet in Co have a high probability of transmission across the interface in the entire energy window shown in Fig. 9(a). This feature is similar to the well-known case of the Co/Cu interface⁷⁵ where the band structure match in the majority-spin channel is nearly perfect.

Because Pt has one electron fewer than Cu and open 5*d* shells, its Fermi surface is more complicated, with one free-electron-like electronic sheet, one extended hole-like sheet that projects to the periphery of the (111) surface Brillouin zone, and one small hole-like pocket around the X point. As the energy is increased, the

hole-like sheets shrink and disappear at about 0.7 eV, where DOS has a van Hove singularity [(see Fig. 9(b)]. The majority-spin transmission $\bar{T}_{\uparrow}^{\text{Co} \rightarrow \text{Pt}}$ is essentially unaffected by the disappearance of the hole-like sheets in Pt, because, as is clear from Figs. 8(a)–8(c), the majority-spin transmission is dominated by electrons from Co transmitting into the electron-like sheet in Pt. On the other hand, $\bar{T}_{\downarrow}^{\text{Co} \rightarrow \text{Pt}}$ decreases significantly in the 0.5–0.7 eV range and remains suppressed up to about 1.0 eV, where it quickly rises to almost 1. The drop around 0.6 eV is associated with the closure of the hole-like sheet in Pt, which decreases the transmission probability of the minority-spin states from Co. The rise at 1.0–1.2 eV is due to the closure of the similar hole-like minority-spin sheets in Co, the electrons from which transmit poorly into Pt but contribute significantly to the Sharvin conductance of Co.

Figure 9(a) shows that the Co/Pt (111) interface has this favorable property in the energy window from 0 to 1.0 eV above the Fermi level, and especially in the 0.6–1.0 eV range, between the top of the 5*d* band of Pt and the top of the minority-spin 3*d* band of Co. Figure 9(c) also shows the spin-resolved effective interfacial area-resistance product calculated according to Schep *et al.*⁷⁵ This quantity represents the apparent spin-dependent resistance of the interface in the circuit under diffusive transport conditions. Although these conditions are not satisfied in THz emission devices, and transport of hot electrons brings its own complications, the spin-dependent effective RA product can serve as an approximate indicator of the interfacial spin asymmetry (noted as the γ parameter). Here, we also see that the Co/Pt (111) interface has a larger effective resistance in the minority-spin channel

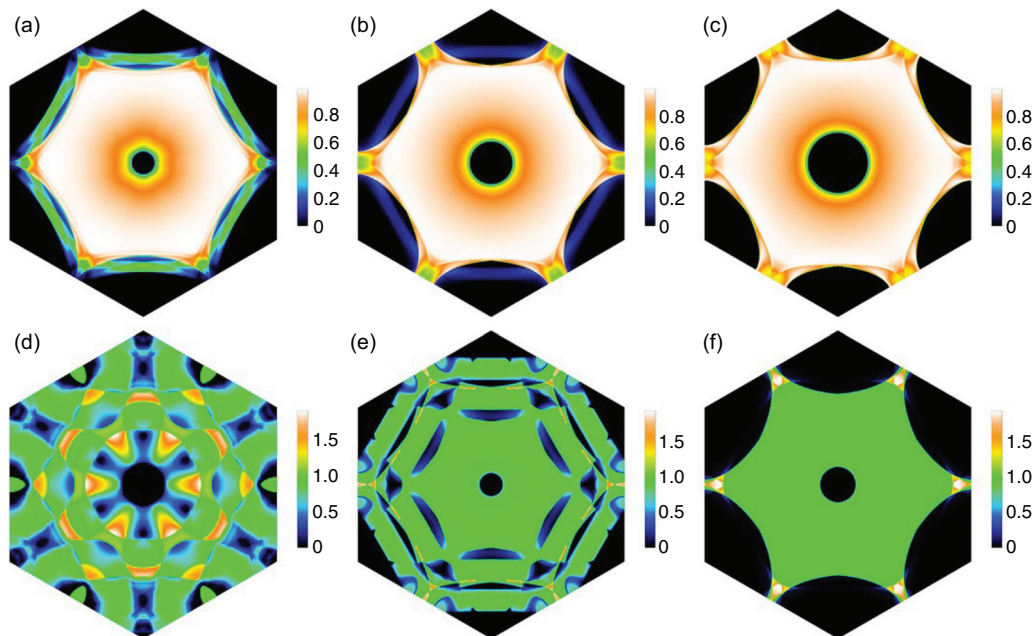


FIG. 8. Calculated energy-dependent and selected-spin transmission function for the Co/Pt (111) interface plotted as a function of \mathbf{k}_{\parallel} (projection of the wave vector on the plane of the interface, which is conserved in the scattering process) and summed in the two-dimensional Brillouin zone of the interface. (a)–(c) Majority-spin channel. (d)–(f) Minority-spin channel. (a) and (d) $E - E_F = 0$. (b) and (e) 0.5 eV. (c) and (f) 1.0 eV. Those calculations show that near the Fermi level [(a)–(d)], the majority electrons (spins \uparrow) are more easily transmitted (on average) than the minority-spin channel (\downarrow), in particular near the Brillouin zone center, whereas at higher energy, 0.5 eV above the Fermi level [(e) and (f)], the electronic transmission for the minority-spin channel is larger (refer to Fig. 9).

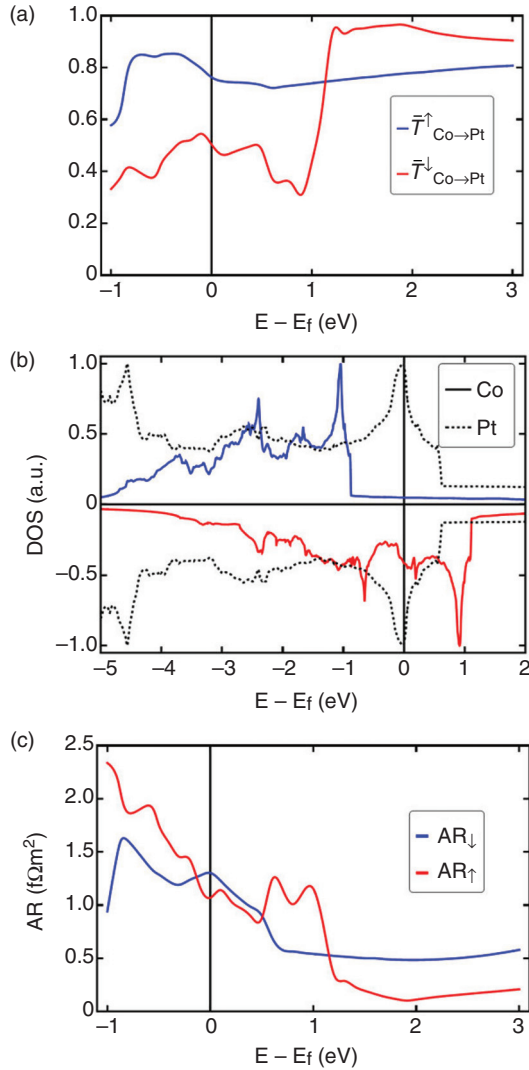


FIG. 9. (a) Spin and energy-dependent average transmission probability for electrons incident from the Co side on the Co/Pt (111) interface, see Eq. (11). Blue (red) lines: majority (minority)-spin electrons. (b) Density of states in bulk fcc Co and Pt with the lattice parameter used in the calculations for the interface. Blue (red) solid lines: majority-spin (minority-spin) electrons in fcc Co. Dotted lines: both spins in Pt. (c) Effective spin- and energy-dependent area-resistance product of the Co/Pt (111) interface. Blue (red) line: majority (minority) spin.

for energies in the 0.6–1.1 eV range that is in the energy region of hot electrons generated by pulsed laser excitations, suggesting an additional “spin-filtering” effect and an enhancement of the spin-current by this interface. Note, however, that the calculation of the spin-selected transmission coefficient per electronic channel [Fig. 9(a)] also shows evidence of a positive spin-asymmetry coefficient near the Fermi level (majority spin \uparrow are favorably transmitted per channel), and such value of $\gamma \approx +0.3$ found here was recently extracted from refined anomalous Hall effect (AHE) experiments and subsequent analyses.⁷⁶

V. RESULTS OF THE NUMERICAL SIMULATIONS

A. FDTD simulations in the time domain

Solving the time-dependent equations requires the implementation of a numerical routine. The experimental boundary conditions corresponding to pulse laser excitation is considered by a zero σ -spin population within the whole multilayers at $t=0$. Additional treatment of the external and internal boundary conditions is available in Appendix C. We have considered a typical temporal Gaussian shape

$$\mathcal{P}_\sigma^0(\mathbf{r}, t) = \mathcal{P}_\sigma^0(t) = s_\sigma \frac{A}{\sqrt{2\pi\Delta t^2}} \exp\left[-\frac{(t - 4\Delta t)^2}{2\Delta t^2}\right] \quad (14)$$

uniformly exciting the ferromagnetic material with a wavelength $\lambda \simeq 810$ nm. A is related to the laser pump power, Δt is the laser pulse duration (typically 100 fs), and s_σ is the initial proportion of the spin-channel excited owing to the different density of states $\mathcal{N}_{d,\sigma}$ of the d -band. *Superdiffusive* spin-currents and secondary electron sources can be performed by adding supplementary nonlinear secondary source terms $\mathcal{P}'_\sigma(\mathbf{r}, t)$ that we do not consider henceforth.

Our numerical investigations will focus on the major role played in the THz wave generation by interfacial transmission T_σ and characteristic spin-flip times to explain the difference between Co/Pt- and NiFe/Au-based samples. In a first step, we will describe the shape of the typical THz spectra. For that end, we consider the change in the spectra obtained by varying, in the same way, both the momentum relaxation time τ_p and the spin-flip time τ_{sf} from their nominal values τ_p^0 and τ_{sf}^0 . We consider the scaling parameter

$$\alpha = \frac{\tau_{sf}}{\tau_{sf}^0} = \frac{\tau_p}{\tau_p^0} \quad (15)$$

in the FM and in the HM material. That permits us to simulate the effect of a typical change of the mobility of the different constituents (Pt- vs Au-based alloys), keeping fixed their spin-orbit parameter $\varepsilon = \frac{\tau_p^0}{\tau_{sf}^0} = \frac{\tau_p}{\tau_{sf}}$. We have previously checked that our simulations give the correct conclusions in the steady-state regime of spin-injection (CW pump).

In order to first explore the strong impact of the transmission T_σ and the observed differences in the Co/Pt and NiFe/Au:W or NiFe/Au:Ta, we consider the spin average transmission T^* and spin-asymmetry γ , as extracted from the *ab initio* calculations

$$T_\sigma = \frac{T^*}{1 \mp \gamma} \Rightarrow T^* = \frac{1 - \gamma^2}{2} (T_\uparrow + T_\downarrow), \quad (16)$$

with $T^* = 0.2$ and $\gamma = +0.5$ at ε_F (Fig. 9). We first make the assumption that the laser pump generates a ratio of spin \uparrow to spin \downarrow equal to 1 : 2 owing to the larger density of states of spin \downarrow electrons at the Fermi level. Figure 10 displays the typical time dependence of

- (1) the out-of-equilibrium spin accumulation or spin-density $m(z=0, t) = n_\uparrow(z=0, t) - n_\downarrow(z=0, t)$ in the HM at the FM/HM interface,
- (2) the corresponding ultrafast charge current $j_c(z=0, t)$ in the HM at the FM/HM interface ($z=0$).
- (3) E_{THz} in the time domain is also plotted in the far-field region. This appears to be in close agreement to both Co(2)/Pt(4) and

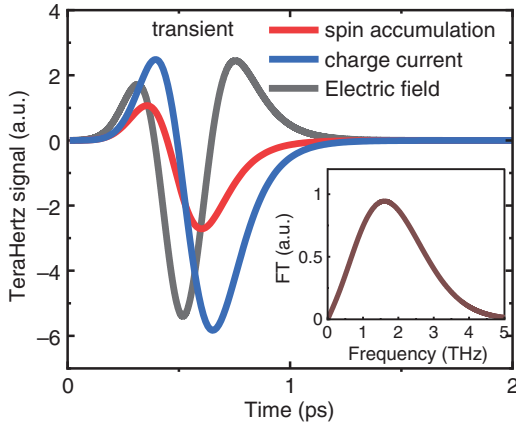


FIG. 10. Typical simulated time-domain evolution of the emitted electric field terahertz signal (gray) calculated for a Co(2)/Pt(4) structure excited by a 100-fs laser pulse in Co. The generated transient ultrafast surface charge current j_c (blue) and out-of-equilibrium spin accumulation (m) (red) are plotted at the interface $z = 0+$ on the Pt side. The Fourier transform (FT) of the corresponding terahertz signal is given in the inset. The typical slope of the FT signal at low frequency is representative of a derivative signal ($E_{THz} \propto \partial j_c / \partial t$). In those simulations, inner average transmission coefficient is $T^* = 0.2$, and the spin interfacial asymmetry was fixed to $\gamma = 0.5$. The other physical parameters are given in Table I.

NiFe(2)/Pt(4) data in shape. The out-of-equilibrium spin-density $m(z = 0, t)$ experiences a maximum around 0.4 ps and a minimum in the vicinity of $t = 0.6$ ps. $m(t)$ gives rise to a maximum (minimum) spin-current gradually converted into an ultrafast charge current by ISHE, j_c . E_{THz} is directly considered as the derivative of the surface charge current j_c integrated within the HM volume. The time response is composed of two small positive lobes surrounding a large negative one resulting from the time-derivative of two Gaussian population functions shifted in time. Regarding the spectral representation of the signal in the frequency domain (see Fig. 10 inset), it covers a wide and continuous band up to 5 THz and fits reasonably well in

form with our experimental data on Co/Pt and NiFe/Pt, taking into account the spectral bandwidth limitation of our detector and experimental IR pulse duration.

B. FDTD simulations in the frequency domain

1. Impact of the electronic transmission

Figure 11 displays the results of our simulated THz spectrum (note the logarithm scale) in the frequency domain using FFT algorithm considering $\gamma = +0.5$. In particular, we have investigated the influence of the inner transmission coefficient T^* at the FM/HM interface for the two different initial spin polarization of the optical pump, either (a) $s_{\uparrow} = 0.5, s_{\downarrow} = 1$ (minority spin favorably pumped) or (b) $s_{\uparrow} = 1, s_{\downarrow} = 0.5$ (majority spin favorably pumped). Relevant information is the intensity ratio between subsequent THz spectra vs T^* . For increasing T^* from 10^{-4} to 0.5, the spectra increases in amplitude by about the same proportion. The THz signal is the largest for $T^* = 0.5$ for both pump polarization that is for either minority [Fig. 11(a)] and majority pumped spins [Fig. 11(b)]. Alongside the difference in their conductivity and in their spin-diffusion length, T^* mainly explains the strong difference in the THz spectra between Co/Pt, NiFe/Pt on one side and NiFe/Au:W or NiFe/Au:Ta on the other side when the transmission for the latter decreases by roughly one order of magnitude (from FMR spin-pumping results). Another important feature is the difference in the signal amplitude [Figs. 11(a) vs 11(b)], about one order of magnitude, on reversing the initial polarization and keeping a fixed $\gamma = +0.5$. This feature indicates a preferential spin-selection (filtering) at the interface allowing a larger THz emission when the preferential pumped spin channel and transmitted spin are equivalent.

2. Effect of material conductivity and spin-flip rate

In Fig. 12, we have explored the effect on the THz spectra of the spin-flip rate in both HM and FM that may be probed in future experiments. One considers here the case of favorably minority spin pumped, $s_{\uparrow} = 0.5$ and $s_{\downarrow} = 1$ and spin-filtering of majority electrons ($\gamma = +0.5$). The typical evolution of THz-TDS spectra resulting from

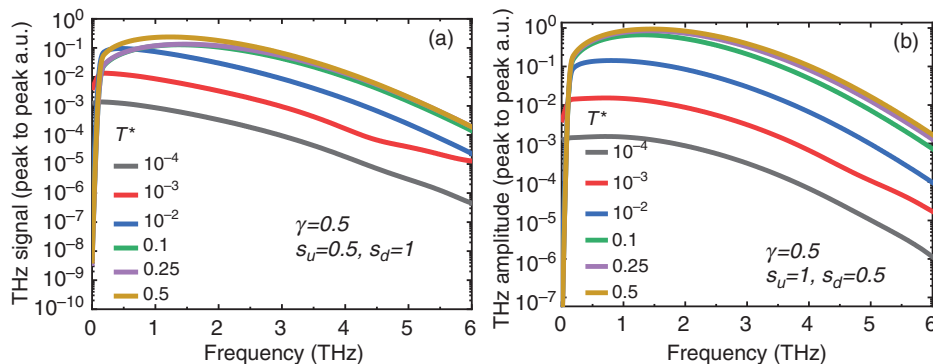


FIG. 11. Simulation results showing the frequency-domain representation (Fourier transform: FT) of the emitted THz electric field spectra E_{THz} (in log scale) in the case of Co(2)/Pt(4) excited by a short 100-fs laser pulse and calculated for different average transmission coefficient from $T^* = 10^{-4}$ to $T = 0.5$. The initial spin polarization was reversed from (a) $s_{\uparrow} = 0.5, s_{\downarrow} = 1$ to (b) $s_{\uparrow} = 1, s_{\downarrow} = 0.5$ while keeping fixed the interfacial spin-asymmetry coefficient $\gamma = +0.5$ through all the simulations. The other physical parameters are given in Table I. Those simulations emphasize the particular role of the so-called interfacial "spin-filtering" effect played by interfaces on the THz spectra.

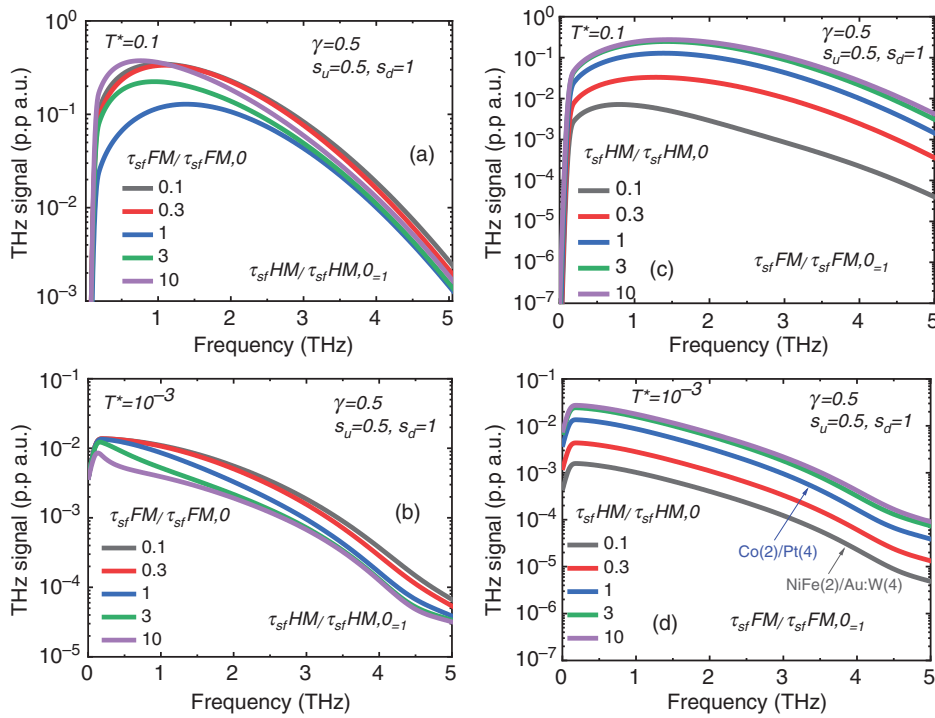


FIG. 12. Frequency-domain representation (FT) of the emitted THz electric field spectra E_{THz} obtained for Co(2)/Pt(4) after a short 100-fs THz laser pulse and considering an initial spin polarization $s_{\uparrow} = 0.5$, $s_{\downarrow} = 1$. The study focuses on the major role played by the spin dynamics timescale change for a fixed transmission parameter respectively equal to $T^* = 10^{-1}$ [(a) and (c)] and $T^* = 10^{-3}$ [(b) and (d)]. Those calculations were performed with respect to the transformation Eq. (D1) for the ferromagnetic layer characterized by a spin scattering time τ_{sf}^{FM} [(a) and (b)] and for the heavy metal characterized by a spin scattering time τ_{sf}^{HM} [(c) and (d)]. The transformation coefficient α is swept in the $[0.1 - 10]$ range. A constant $\gamma = +0.5$ value was kept for the whole simulations.

a pump pulse of 100 fs on varying $\alpha = 0.1, 0.3, 1, 3, 10$ in FM and HM are reported on respective Figs. 12(a) and 12(b) and Figs. 12(c) and 12(d) for $T^* = 10^{-1}$ [Figs. 12(a) and 12(c)] and $T^* = 10^{-3}$ [Figs. 12(b) and 12(d)]. Two major conclusions can be raised. Concerning the dependence on α_{FM} , and for $T^* = 0.1$ [Fig. 12(a)], one notes a significant increase in the THz signal while increasing α_{FM} from 0.1 to 10 as already pointed out. However, this conclusion is exactly opposite in the case of a small transmission $T^* = 10^{-3}$, mainly because the spin-filtering acts in an opposite way to the optical pumping. This yields a reduction of the spin-population in FM and then in the THz spectra [Fig. 12(a) vs Fig. 12(b)]. Second, a slight increase in the signal due to spin-flip in FM makes the spin-filtering effect more efficient.

On the other hand, increasing the α_{HM} ratio increases the amplitude of the THz spectra [Figs. 12(c) and 12(d)] owing to a higher mobility, leading to a larger spin-diffusion length and larger volume of charge relaxation in HM. In this sense, we demonstrate here the relationship given by Eq. (9) by which E_{THz} follows the local HM conductivity (or HM mobility) in proportion to α_{HM} . This feature is clearly demonstrated in Figs. 12(c) and 12(d) whatever T^* is and also evidenced experimentally when comparing (Co,NiFe)/Pt- and NiFe/Au-based alloys. Note that the change of α_{HM} does not imply a variation of the spin-orbit parameter (ϵ_{HM}), avoiding thus the possible effect of the so-called impedance mismatch between FM and HM.

VI. CONCLUSIONS

To conclude, we have demonstrated strong THz pulse emission from Co(2)/Pt(4) and NiFe(2)/Pt(4) transition metal bilayers, mediated by inverse spin-Hall effect in the time domain. Such emission is of dipolar origin and leads to an almost full linear polarization of the

electric emitted field. In Pt-based interfaces, the THz emission is shown to be much larger, by more than one order of magnitude, than that provided by NiFe/Au:W or NiFe/Au:Ta alloys via their *extrinsic* ISHE. The difference in the emission efficiency is partly explained from the difference in the resistivity. From our transport simulations, it indeed follows that the optimization of the THz emission requires a maximum spin-Hall angle (SHA) θ_{SHE} , spin-diffusion length l_{sf} , and electronic transmission T^* , together with a reduced resistivity. It seems that the product $(\theta_{SHE} \sigma_{xx} l_{sf} T^*)$ constitutes the correct figure of merit for charge conversion in the time-domain. This explains the difference observed between (Co,NiFe)/Pt- and NiFe/Au:W- or NiFe/Au:Ta-based alloys. The above considerations suggest that the performance of the Co/Pt (111) THz emission devices can be increased further by widening the high-asymmetry window between the top of the Pt 5d band and the top of the minority-spin Co 3d band, while maintaining the large spin-Hall angle in the heavy metal. A natural way to achieve this is to alloy Pt with another element with a higher electron count, such as Au, and to use a ferromagnetic alloy with a larger exchange splitting compared to Co, such as the Fe-Co alloys near the apex of the Slater-Pauling curve. Moreover, THz emission spectroscopy methods applied to spintronics structures using the inverse spin-Hall effect and/or the inverse Edelstein effect may prove to be a very efficient method to determine the spin injection properties at the nanoscale or in quantum surface states, also to determine the local spin-conductivity within multilayers as performed in standard non-magnetic layers.⁸³

ACKNOWLEDGMENTS

We acknowledge financial support from the Horizon 2020 Framework Programme of the European Commission under FET-

Open Grant No. 863155 (s-Nebula). T.-H. Dang acknowledges the Horizon 2020 Framework Programme of the European Commission under FET-Proactive Grant No. 824123 (SKYTOP). The work at UNL was supported by the National Science Foundation (NSF) through Grant Nos. DMR-1609776 and DMR-1916275 and the Nebraska Materials Research Science and Engineering Center (MRSEC, Grant No. DMR-1420645). Calculations were performed utilizing the Holland Computing Center of the University of Nebraska, which receives support from the Nebraska Research Initiative.

APPENDIX A: FROM CONTINUOUS PUMPING TO PULSE EXCITATION

Here, we develop the fundamentals of hot spin-carrier injection in the limit of a continuous pumping (steady-state regime of injection) considering characteristic interface transmission and material spin-flip resistances before discussing the case of pulse excitation. We consider (1) the spin-injection problem whereby the spin-current is controlled in the FM material far from the interface and (2) the spin-pumping problem corresponding to a constant out-of-equilibrium spin-accumulation at the FM side. The case of a (3) pulsed laser spin-injection will correspond to an intermediate situation combining spin-accumulation and spin-current injections owing its time-domain property.

1. Electrical spin-injection

Concerning the electrical injection issue, the efficiency of spin-injection η_j may be defined by the ratio between the spin-current j_s^I injected at the interface (designed as I) over its maximum value given in the bulk material j_s^∞ . It writes

$$\eta_j = \frac{j_s^I}{j_s^\infty} = \frac{g_s r_{FM}}{1 + g_s (r_{FM} + r_{HM})} \simeq \frac{T^* \sqrt{\frac{\tau_{sf}^{FM}}{\tau_{FM}}}}{1 + T^* \left(\sqrt{\frac{\tau_{sf}^{FM}}{\tau_{FM}}} + \sqrt{\frac{\tau_{sf}^{HM}}{\tau_{HM}}} \right)} \quad (\text{A1})$$

where $g_s = \frac{e^2}{h} \sum_{k_{\parallel}} T(k_{\parallel})$ is the typical surface conductance; r_s^{FM} and r_s^{HM} are the spin-resistances of FM and HM, respectively; and $r_s = \rho \times l_{sf} \propto \sqrt{\frac{\tau_{sf}}{\tau_p}}$ is the product of the resistivity by the spin-diffusion length. In the previous expression, τ_p and τ_{sf} are the characteristic momentum relaxation time and spin-flip time, whereas $\varepsilon = \frac{\tau_p}{\tau_{sf}}$ can be defined as the spin-orbit parameter (probability of spin-flip after diffusion). The spin-resistance represents the resistance to spin-flip. T^* is the average electron transparency over the different incoming channel k_{\parallel} . Equation (A1), involving spin-flip times, reflects the proportion of time spent by the carriers in each material separately and weighted by the interface transmission once generated in the FM side. In the limit of the small transparency, the efficiency of spin-injection is found to be small. Moreover, one notes that η_j depends strongly on the spin-flip rate in FM, a shorter τ_{sf} leading to a smaller spin-injection.

2. Case of FMR spin-pumping

In the case of spin-pumping providing a constant spin-accumulation level in FM of the order of $\Delta\mu \simeq \hbar\omega \sin^2\theta_M$, with ω

as the rf frequency and θ_M the mean precession angle of the magnetization around its equilibrium position, one obtains a spin-injection efficiency η_μ given by

$$\eta_\mu = \frac{j_s^I}{\Delta\mu^0} = \frac{g_s}{1 + g_s r_s^{HM}} \simeq \frac{T^*}{1 + T^* \sqrt{\frac{\tau_{sf}^{HM}}{\tau_{HM}}}}. \quad (\text{A2})$$

The efficiency of spin-injection in spin-pumping only depends on the rate of spin-flips in HM and is insensitive to the amount of spin-flip in FM unlike the electrical injection problem. We come to the conclusion that the spin-pumping injection is more robust to material properties, in particular, to the properties and spin-flips of the FM material, but still dependent of the interface transparency T^* .

3. Laser pulse injection

Because it occurs in the time-domain window, the laser pulse injection is controlled by both the spin-current and spin-accumulation. Consequently, the spin-injection efficiency should reveal an intermediate behavior between the electrical and spin-pumping situations. This is what is investigated in the following.

APPENDIX B: TIME DYNAMICS

In the limit $t < \tau_r$, these coupled equations lead to the determination of both out-of-equilibrium magnetization (the so-called spin-accumulation) $m = n_{\uparrow} - n_{\downarrow}$ and spin-current $j_s = j_{\uparrow} - j_{\downarrow}$ via the following second-order differential equations:

$$\begin{aligned} \frac{\partial^2 m}{\partial t^2} + \left[\frac{1}{\tau_{sf}} + \frac{\delta_{i,L}}{\tau_r} \right] \frac{\partial m}{\partial t} - \frac{1}{\tilde{\tau}} \frac{\partial j_s}{\partial z} - \frac{\tilde{D}}{\tilde{\tau}} \frac{\partial^2 m}{\partial z^2} &= \frac{\partial \mathcal{P}}{\partial t} \delta_{i,L} \\ \frac{\partial^2 j_s}{\partial t^2} + \frac{1}{\tilde{\tau}} \frac{\partial j_s}{\partial t} - \frac{\tilde{D}}{\tilde{\tau}} \left[\frac{1}{\tau_{sf}} + \frac{\delta_{i,L}}{\tau_r} \right] \frac{\partial m}{\partial z} - \frac{\tilde{D}}{\tilde{\tau}} \frac{\partial^2 j_s}{\partial z^2} &= -\frac{\tilde{D}}{\tilde{\tau}} \frac{\partial \mathcal{P}}{\partial z} \delta_{i,L} \end{aligned}$$

or equivalently

$$\frac{\partial^2 m}{\partial t^2} + \left[\frac{1}{\tau} + \frac{1}{\tau_{sf}} \right] \frac{\partial m}{\partial t} + \frac{m}{\tau \tau_{sf}} - \frac{\tilde{D}}{\tau} \frac{\partial^2 m}{\partial z^2} = \frac{\partial \mathcal{P}}{\partial t} \quad (\text{B1})$$

$$\frac{\partial^2 j_s}{\partial t^2} + \left[\frac{1}{\tau} + \frac{1}{\tau_{sf}} \right] \frac{\partial j_s}{\partial t} + \frac{j_s}{\tau \tau_{sf}} - \frac{\tilde{D}}{\tau} \frac{\partial^2 j_s}{\partial z^2} = -\frac{\tilde{D}}{\tau} \frac{\partial \mathcal{P}}{\partial z} \quad (\text{B2})$$

for large τ_r . $\tilde{D} = \frac{2D_{\uparrow}D_{\downarrow}}{D_{\uparrow}+D_{\downarrow}}$ is the average diffusion constant, $\tilde{\tau} = \frac{2\tau_{\uparrow}\tau_{\downarrow}}{\tau_{\uparrow}+\tau_{\downarrow}}$ is average scattering time, and $\mathcal{P} = \mathcal{P}_{\uparrow} - \mathcal{P}_{\downarrow}$ is the time-profile of the spin-polarized pump.

APPENDIX C: BOUNDARY CONDITIONS FOR SPIN-POLARIZED HOT CARRIERS

In order to establish the dynamics of spin-currents within the bilayers, we must introduce the specific boundary conditions. These consist of the continuity of the spin-current j_s at the inner bilayer interface ($z=0$ by definition) at any time t once spin-flips and spin decoherence have been neglected. For a given spin channel σ , the related current densities at both sides are related to the spin

population n_σ in both regions and to their characteristic transfer velocity $v_{\sigma\sigma'}^I$ by

$$\begin{aligned} j_\sigma^L(z=0^-, t) &= v_{\sigma\sigma'}^I [n_\sigma^L(z=0^-, t) - n_\sigma^R(z=0^+, t)] \\ &\quad + v_{\uparrow\downarrow}^I [n_\sigma^L(z=0^-, t) - n_\sigma^R(z=0^+, t)] \\ j_\sigma^R(z=0^+, t) &= v_{\sigma\sigma'}^I [n_\sigma^L(z=0^-, t) - n_\sigma^R(z=0^+, t)] \\ &\quad + v_{\uparrow\downarrow}^I [n_\sigma^L(z=0^-, t) - n_\sigma^R(z=0^+, t)], \end{aligned} \quad (C1)$$

where the transfer velocity $v_{\sigma\sigma'}^I$ writes $v_{\sigma\sigma'}^I = v_F T^{\sigma\sigma'}$ linked to the interface conductance $g_{\sigma\sigma'}^I$ and density of states \mathcal{N}_E by $g_{\sigma\sigma'}^I = \frac{e^2}{2\pi} \mathcal{N}_E v_{\sigma\sigma'}^I$. In that sense, $\frac{\sqrt{2}T^{\uparrow\downarrow}}{\sqrt{T^{\uparrow\uparrow}+T^{\downarrow\downarrow}}}$ may be viewed as the probability of spin-flip p_{sf} . From Eq. (C1), we note that $j_\uparrow^L + j_\downarrow^L = j_\uparrow^R + j_\downarrow^R$ manifests the current continuity at the inner interface I , whereas $j_s^L - j_s^R = (j_\uparrow^L - j_\uparrow^R) - (j_\downarrow^L - j_\downarrow^R) = 2v_{\uparrow\downarrow}^I(m^L + m^R)$ is the condition for the spin-current discontinuity with $m^{L,R} = n_\uparrow^{L,R} - n_\downarrow^{L,R}$ the spin accumulation at both sides. We consider pure specular reflections (i.e., $R=1$) on the two external surfaces located at $z = z_B^\pm$ (left - and right + limits). This leads to

$$\begin{aligned} n_\sigma^{\text{out}}(z_B^\pm, t) &= \left(1 - \frac{p_{sf}}{2}\right) n_\sigma^{\text{in}} + \frac{p_{sf}}{2} n_\sigma^{\text{in}} \\ j_c(z = z_B^\pm, t) &= j_\uparrow(z = z_B^\pm, t) + j_\downarrow(z = z_B^\pm, t) = 0 \\ j_s(z = z_B^\pm, t) &= j_\uparrow(z = z_B^\pm, t) - j_\downarrow(z = z_B^\pm, t) \\ &= \frac{p_{sf}}{2 - p_{sf}} \times [m(z = z_B^\pm, t)] \left(\frac{v_{F,\uparrow} + v_{F,\downarrow}}{2}\right) \end{aligned} \quad (C2)$$

considering p_{sf} as the probability of spin-flip after scattering on the outer surfaces. Note that inside the non-magnetic layer, the carrier velocity is spin-independent.

APPENDIX D: MODELING OF SPIN-TRANSPORT IN THE STEADY-STATE (CONTINUOUS PUMPING)

In order to analyze our results, we consider the following homothetic time transformation:

$$\tau'_\sigma \rightarrow \alpha \tau_\sigma \quad \text{and} \quad \tau'_{sf} \rightarrow \alpha \tau_{sf} \quad (D1)$$

scaled by a unitless α parameter defined in each region (FM/HM) separately. We consider here the case of a continuous laser pump in FM in the particular case of a low-transmission T limit at the FM/HM interface. We present on Fig. 13 the calculated spin accumulation (or spin-density) profile along z , $m(z)$ [Figs. 13(a) and 13(c)] alongside the spin-current profile $j_s(z)$ [Figs. 13(b) and 13(d)] after a long delay time (30 ps). The electronic parameters for both materials (FM/HM = Co/Pt) are gathered in Table I. The sample is typically Co(10)/Pt(4). We have lowered the transmission coefficient T^* down to 10^{-3} and considered a null interface transmission spin-asymmetry $\gamma=0$ to simplify. The laser pump is continuously on [i.e., $\mathcal{P}_\sigma(t) = \mathcal{P} = A s_\sigma$] with the result that only hot spin-up population is generated ($s_\uparrow = 1$ and $s_\downarrow = 0$). In this simulation, we emphasize the respective roles of τ_{sf}^{FM} [Figs. 13(a) and 13(b)] and τ_{sf}^{HM} [Figs. 13(c) and 13(d)].

One notes several interesting features making the problem particularly singular. First, if one varies $\alpha_{FM} = \frac{\tau_{sf}^{FM}}{\tau_{sf}^{FM,0}}$ by two orders of magnitudes from 0.1 to 10, one notes a strong change in the level of the spin population saturating to a constant value inside the FM [Fig. 13(a)]. The value at saturation of the spin-density population $\Delta\mu \propto m = n_\uparrow - n_\downarrow$ in FM increases quasi-linearly with α_{FM} owing to the corresponding increase in the spin-relaxation time. Thus, FM plays the role of a cavity or spin-reservoir with a particle level fixed

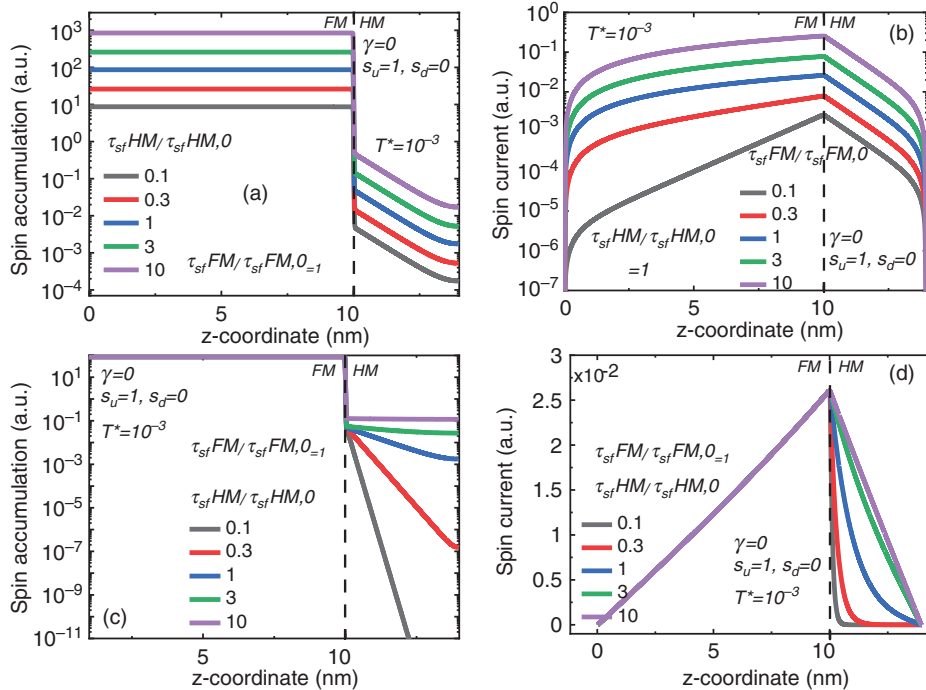


FIG. 13. Confined case simulation considering a ferromagnetic continuous pumping with $s_\uparrow = 1$ and $s_\downarrow = 0$ on a Co(10)/Pt(4) modeled sample. Spin accumulations m [(a) and (c)] and spin-currents j_s [(b) and (d)] are presented for long-time approximation by respectively varying τ_{sf}^{FM} [(a) and (b)] and τ_{sf}^{HM} [(c) and (d)]. The interface between the heavy metal and the ferromagnetic layer is modeled using a spin interfacial asymmetry $\gamma=0$ and a coefficient transmission $T^* = 10^{-3}$.

by their characteristic spin-flip time. Correspondingly, in HM, the spin population decreases typically by a factor 10^{-3} . The spin accumulation in HM decreases in proportion to that in FM and to the electronic transmission T^* . The spatial decrease in the spin-population profile in HM remains insensitive to the α_{FM} parameter because the spin-diffusion length in HM remains fixed. The spatial dependence of spin population and spin-current remains unaffected in HM. In the limit of small electron transparency, the spin-current space profile $j_s(z)$ calculated by considering the continuity of the spin-current at the inner interface and a zero spin-current at the edges of the materials follows the same typical decrease than the spin density [Fig. 13(b)].

Figures 13(c) and 13(d) display the equivalent space profiles when $\alpha_{HM} = \frac{\tau_{sf}^{HM}}{\tau_{sf}^{FM}}$ is changed in the same way, from 0.1 to 10, keeping fixed the parameters in the FM layer and still for a small electronic transparency $T = 10^{-3}$. Profiles are taken at a time $t = 30$ ps. The differences are noticeable from the previous case. The level of spin population in FM now remains constant due to the fixed value $\tau_{sf}^{FM} = \tau_{sf}^{FM,0}$. The spin-current in FM admits a constant profile characterized by a same value at the two FM interfaces [$j_s = 0$ to the left and $j_s \approx 2.6$ (a.u.) at the FM/HM interface]. The main changes with varying α_{HM} are now related to the space-varying profile of both spin-accumulation $m(z)$ and spin-current $j_s(z)$ in HM due to the conjugate variation of τ_{sf}^{HM} and τ_{HM} . Those space-profile lengthscales are now governed by the effective spin diffusion length $l_{sf}^{HM} = \sqrt{D_{HM}\tau_{sf}^{HM}} \propto \alpha_{HM}$ as expected before saturating to a value close to the thickness l_{HM} owing to the boundary condition chosen ($j_s = 0$ at the outward boundaries, in particular, at the right boundary of Pt).

DATA AVAILABILITY

The data that support the findings of this study are available within the article and its Appendixes.

REFERENCES

- S. S. Dhillon, M. S. Vitiello, E. H. Linfield, A. G. Davies *et al.*, "The 2017 terahertz science and technology roadmap," *J. Phys. D: Appl. Phys.* **50**, 043001 (2017).
- S.-C. Chen, Z. Feng, J. Li, W. Tan, L.-H. Du, J. Cai, Y. Ma, K. He, H. Ding, Z.-H. Zhai, Z.-R. Li, C.-W. Qiu, X.-C. Zhang, and L.-G. Zhu, "Ghost spintronic THz-emitter-array microscope," *Light Sci. Appl.* **9**, 99 (2020).
- D. J. Hilton, R. D. Averitt, C. A. Meserole, G. L. Fisher, D. J. Funk, J. D. Thompson, and A. J. Taylor, "Terahertz emission via ultrashort-pulse excitation of magnetic metal films," *Opt. Lett.* **29**, 1805–1807 (2004).
- T. Seifert, S. Jaiswal, U. Martens, J. Hannegan, L. Braun, P. Maldonado, F. Freimuth, A. Kronenberg, J. Henrizi, I. Radu *et al.*, "Efficient metallic spintronic emitters of ultrabroadband terahertz radiation," *Nature Photonics* **10**, 483–488 (2016).
- E. Beaurepaire, J.-C. Merle, A. Daunois, and J.-Y. Bigot, "Ultrafast spin dynamics in ferromagnetic nickel," *Phys. Rev. Lett.* **76**, 4250–4253 (1996).
- B. Koopmans, M. van Kampen, J. T. Kohlhepp, and W. J. M. de Jonge, "Ultrafast magneto-optics in nickel: Magnetism or optics?," *Phys. Rev. Lett.* **85**, 844–847 (2000).
- E. Beaurepaire, G. M. Turner, S. M. Harrel, M. C. Beard, J.-Y. Bigot, and C. A. Schmuttenmaer, "Coherent terahertz emission from ferromagnetic films excited by femtosecond laser pulses," *Appl. Phys. Lett.* **84**, 3465 (2004).
- A. Melnikov, I. Razdolski, T. O. Wehling, E. T. Papaioannou, V. Roddatis, P. Fumagalli, O. Aksipetrov, A. I. Lichtenstein, and U. Bovensiepen, "Ultrafast transport of laser-excited spin-polarized carriers in Au/Fe/MgO(001)," *Phys. Rev. Lett.* **107**, 076601 (2011).
- T. J. Huisman, R. V. Mikhaylovskiy, A. Tsukamoto, T. Rasing, and A. V. Kimel, "Simultaneous measurements of terahertz emission and magneto-optical Kerr effect for resolving ultrafast laser-induced demagnetization dynamics," *Phys. Rev. B* **92**, 104419 (2015).
- Z. Jin, A. Tkach, F. Casper, V. Spetter, H. Grimm, A. Thomas, T. Kampfrath, M. Bonn, M. Kläui, and D. Turchinovich, "Accessing the fundamentals of magnetotransport in metals with terahertz probes," *Nat. Phys.* **11**, 761–766 (2015).
- T. J. Huisman, R. V. Mikhaylovskiy, J. D. Costa, F. Freimuth, E. Paz, J. Ventura, P. P. Freitas, S. Blügel, Y. Mokrousov, T. Rasing, and A. V. Kimel, "Femtosecond control of electric currents in metallic ferromagnetic heterostructures," *Nat. Nanotechnol.* **11**, 455–458 (2016).
- D. Yang, J. Liang, C. Zhou, L. Sun, R. Zheng, S. Luo, Y. Wu, and J. Qi, "Powerful and tunable THz emitters based on the Fe/Pt magnetic heterostructure," *Adv. Opt. Mater.* **4**, 1944–1949 (2016).
- E. Saitoh, M. Ueda, H. Miyajima, and G. Tatara, "Conversion of spin current into charge current at room temperature: Inverse spin-Hall effect," *Appl. Phys. Lett.* **88**, 182509 (2006).
- A. Hoffmann, "Spin Hall effects in metals," *IEEE Trans. Magn.* **49**, 5172–5193 (2013).
- J. Sinova, S. O. Valenzuela, J. Wunderlich, C. H. Back, and T. Jungwirth, "Spin Hall effects," *Rev. Mod. Phys.* **87**, 1213–1260 (2015).
- G. Y. Guo, S. Murakami, T.-W. Chen, and N. Nagaosa, "Intrinsic spin Hall effect in platinum: First-principles calculations," *Phys. Rev. Lett.* **100**, 096401 (2008).
- T. Tanaka, H. Kontani, M. Naito, T. Naito, D. S. Hirashima, K. Yamada, and J. Inoue, "Intrinsic spin Hall effect and orbital Hall effect in 4d and 5d transition metals," *Phys. Rev. B* **77**, 165117 (2008).
- V. Edelstein, "Spin polarization of conduction electrons induced by electric current in two-dimensional asymmetric electron systems," *Solid State Communications* **73**, 233–235 (1990).
- J. C. R. Sánchez, L. Vila, G. Desfonds, S. Gambarelli, J. P. Attané, J. M. De Teresa, C. Magén, and A. Fert, "Spin-to-charge conversion using Rashba coupling at the interface between non-magnetic materials," *Nat. Commun.* **4**, 2944 (2013).
- C. Zhou, Y. P. Liu, Z. Wang, S. J. Ma, M. W. Jia, R. Q. Wu, L. Zhou, W. Zhang, M. K. Liu, Y. Z. Wu, and J. Qi, "Broadband terahertz generation via the interface inverse Rashba-Edelstein effect," *Phys. Rev. Lett.* **121**, 086801 (2018).
- M. B. Jungfleisch, Q. Zhang, W. Zhang, J. E. Pearson, R. D. Schaller, H. Wen, and A. Hoffmann, "Control of terahertz emission by ultrafast spin-charge current conversion at Rashba interfaces," *Phys. Rev. Lett.* **120**, 207207 (2018).
- X. Wang, L. Cheng, D. Zhu, Y. Wu, M. Chen, Y. Wang, D. Zhao, C. B. Boothroyd, Y. M. Lam, J.-X. Zhu, M. Battiato, J. C. W. Song, H. Yang, and E. E. M. Chia, "Ultrafast spin-to-charge conversion at the surface of topological insulator thin films," *Adv. Mater.* **30**, 1802356 (2018).
- M. T. Hibberd, D. S. Lake, N. A. B. Johansson, T. Thomson, S. P. Jamison, and D. M. Graham, "Magnetic-field tailoring of the terahertz polarization emitted from a spintronic source," *Appl. Phys. Lett.* **114**, 031101 (2019).
- B. Wang, S. Shan, X. Wu, C. Wang, C. Pandey, T. Nie, W. Zhao, Y. Li, J. Miao, and L. Wang, "Picosecond nonlinear spintronic dynamics investigated by terahertz emission spectroscopy," *Appl. Phys. Lett.* **115**, 121104 (2019).
- Y. Wu, M. Elyasi, X. Qiu, M. Chen, Y. Liu, L. Ke, and H. Yang, "High-performance THz emitters based on ferromagnetic/nonmagnetic heterostructures," *Adv. Mater.* **29**, 1603031 (2017).
- T. Seifert, S. Jaiswal, M. Sajadi, G. Jakob, S. Winnerl, M. Wolf, M. Kläui, and T. Kampfrath, "Ultrabroadband single-cycle terahertz pulses with peak fields of 300 kV cm⁻¹ from a metallic spintronic emitter," *Appl. Phys. Lett.* **110**, 252402 (2017).
- T. S. Seifert, N. M. Tran, O. Gueckstock, S. M. Rouzgar, L. Nadvornik, S. Jaiswal, G. Jakob, V. V. Temnov, M. Münzenberg, M. Wolf, M. Kläui, and T. Kampfrath, "Terahertz spectroscopy for all-optical spintronic characterization of the spin-Hall-effect metals Pt, W and Cu₈₀Ir₂₀," *J. Phys. D: Appl. Phys.* **51**, 364003 (2018).
- G. Torosyan, S. Keller, L. Scheuer, R. Beigang, and E. T. Papaioannou, "Optimized spintronic terahertz emitters based on epitaxial grown Fe/Pt layer structures," *Sci. Rep.* **8**, 1311 (2018).

- ²⁹H. S. Qiu, K. Kato, K. Hirota, N. Sarukura, M. Yoshimura, and M. Nakajima, "Layer thickness dependence of the terahertz emission based on spin current in ferromagnetic heterostructures," *Opt. Express* **26**, 15247–15254 (2018).
- ³⁰J. Cramer, T. Seifert, A. Kronenberg, F. Fuhrmann, G. Jakob, M. Jourdan, T. Kampfrath, and M. Kläui, "Complex terahertz and direct current inverse spin Hall effect in YIG/Cu_{1-x}Lrx bilayers across a wide concentration range," *Nano Lett.* **18**, 1064–1069 (2018).
- ³¹R. I. Herapath, S. M. Hornett, T. S. Seifert, G. Jakob, M. Kläui, J. Bertolotti, T. Kampfrath, and E. Hendry, "Impact of pump wavelength on terahertz emission of a cavity-enhanced spintronic trilayer," *Appl. Phys. Lett.* **114**, 041107 (2019).
- ³²M. Chen, Y. Wu, Y. Liu, K. Lee, X. Qiu, P. He, J. Yu, and H. Yang, "Current-enhanced broadband THz emission from spintronic devices," *Adv. Opt. Mater.* **7**, 1801608 (2019).
- ³³Z. Feng, R. Yu, Y. Zhou, H. Lu, W. Tan, H. Deng, Q. Liu, Z. Zhai, L. Zhu, J. Cai, B. Miao, and H. Ding, "Highly efficient spintronic terahertz emitter enabled by metal–dielectric photonic crystal," *Adv. Opt. Mater.* **6**, 1800965 (2018).
- ³⁴L. Zhu, D. C. Ralph, and R. A. Buhrman, "Enhancement of spin transparency by interfacial alloying," *Phys. Rev. B* **99**, 180404 (2019).
- ³⁵L. Zhu, L. Zhu, S. Shi, M. Sui, D. C. Ralph, and R. A. Buhrman, "Enhancing spin-orbit torque by strong interfacial scattering from ultrathin insertion layers," *Phys. Rev. Appl.* **11**, 061004 (2019).
- ³⁶L. Zhu and R. Buhrman, "Maximizing spin-orbit-torque efficiency of Pt/Ti multilayers: Trade-off between intrinsic spin Hall conductivity and carrier lifetime," *Phys. Rev. Appl.* **12**, 051002 (2019).
- ³⁷H.-Y. Lee, S. Kim, J.-Y. Park, Y.-W. Oh, S.-Y. Park, W. Ham, Y. Kotani, T. Nakamura, M. Suzuki, T. Ono, K.-J. Lee, and B.-G. Park, "Enhanced spin-orbit torque via interface engineering in Pt/CoFeB/MgO heterostructures," *APL Materials* **7**, 031110 (2019).
- ³⁸J.-C. Rojas-Sánchez, N. Reyren, P. Laczkowski, W. Savero, J.-P. Attané, C. Deranlot, M. Jamet, J.-M. George, L. Vila, and H. Jaffrès, "Spin pumping and inverse spin Hall effect in platinum: The essential role of spin-memory loss at metallic interfaces," *Phys. Rev. Lett.* **112**, 106602 (2014).
- ³⁹A. J. Berger, E. R. J. Edwards, H. T. Nembach, O. Karis, M. Weiler, and T. J. Silva, "Determination of the spin Hall effect and the spin diffusion length of Pt from self-consistent fitting of damping enhancement and inverse spin-orbit torque measurements," *Phys. Rev. B* **98**, 024402 (2018).
- ⁴⁰K. D. Belashchenko, A. A. Kovalev, and M. van Schilfgaarde, "Theory of spin loss at metallic interfaces," *Phys. Rev. Lett.* **117**, 207204 (2016).
- ⁴¹K. Dolui and B. K. Nikolić, "Spin-memory loss due to spin-orbit coupling at ferromagnet/heavy-metal interfaces: *Ab initio* spin-density matrix approach," *Phys. Rev. B* **96**, 220403 (2017).
- ⁴²M. Zeng, B. Chen, and S. T. Lim, "Interfacial electric field and spin-orbitronic properties of heavy-metal/CoFe bilayers," *Appl. Phys. Lett.* **114**, 012401 (2019).
- ⁴³R. J. H. Wesselink, K. Gupta, Z. Yuan, and P. J. Kelly, "Calculating spin transport properties from first principles: Spin currents," *Phys. Rev. B* **99**, 144409 (2019).
- ⁴⁴K. Gupta, R. J. H. Wesselink, R. Liu, Z. Yuan, and P. J. Kelly, "Disorder dependence of interface spin memory loss," *Phys. Rev. Lett.* **124**, 087702 (2020).
- ⁴⁵L. Liu, T. Moriyama, D. C. Ralph, and R. A. Buhrman, "Spin-torque ferromagnetic resonance induced by the spin Hall effect," *Phys. Rev. Lett.* **106**, 036601 (2011).
- ⁴⁶W. Zhang, W. Han, X. Jiang, S.-H. Yang, and S. S. P. Parkin, "Role of transparency of platinum–ferromagnet interfaces in determining the intrinsic magnitude of the spin Hall effect," *Nat. Phys.* **11**, 496–502 (2015).
- ⁴⁷A. Okada, Y. Takeuchi, K. Furuya, C. Zhang, H. Sato, S. Fukami, and H. Ohno, "Spin-pumping-free determination of spin-orbit torque efficiency from spin-torque ferromagnetic resonance," *Phys. Rev. Appl.* **12**, 014040 (2019).
- ⁴⁸A. Ciuciułkaite, O. Gueckstock, A. Ravensburg, M. Pohlitz, T. Warnatz, T. Kampfrath, G. Schmidt, E. T. Papaioannou, and V. Kapaklis, "Enhanced THz emission from spintronic Fe/Pt emitters through crystal growth optimization," *arXiv:2010.12457v1* (2020).
- ⁴⁹D. M. Nenko, L. Scheuer, D. Sokoluk, S. Keller, G. Torosyan, A. Brodyanski, J. Lösch, M. Battiato, M. Rahm, R. H. Binder, H. C. Schneider, R. Beigang, and E. T. Papaioannou, "Modification of spintronic terahertz emitter performance through defect engineering," *Sci. Rep.* **9**, 13348 (2019).
- ⁵⁰W.-T. Lu, Y. Zhao, M. Battiato, Y. Wu, and Z. Yuan, "Interface reflectivity of a superdiffusive spin current in ultrafast demagnetization and terahertz emission," *Phys. Rev. B* **101**, 014435 (2020).
- ⁵¹E. Lesne, Y. Fu, S. Oyarzun, J. C. Rojas-Sánchez, D. C. Vaz, H. Naganuma, G. Sicoli, J.-P. Attané, M. Jamet, E. Jacquet, J.-M. George, A. Barthélémy, H. Jaffrès, A. Fert, M. Bibes, and L. Vila, "Highly efficient and tunable spin-to-charge conversion through Rashba coupling at oxide interfaces," *Nat. Mater.* **15**, 1261–1266 (2016).
- ⁵²J.-C. Rojas-Sánchez, P. Laczkowski, J. Sampaio, S. Collin, K. Bouzehouane, N. Reyren, H. Jaffrès, A. Mougin, and J.-M. George, "Perpendicular magnetization reversal in Pt/[Co/Ni]₃/Al multilayers via the spin Hall effect of Pt," *Appl. Phys. Lett.* **108**, 082406 (2016).
- ⁵³P. Laczkowski, J.-C. Rojas-Sánchez, W. Savero-Torres, H. Jaffrès, N. Reyren, C. Deranlot, L. Notin, C. Beigné, A. Marty, J.-P. Attané, L. Vila, J.-M. George, and A. Fert, "Experimental evidences of a large extrinsic spin Hall effect in AuW alloy," *Appl. Phys. Lett.* **104**, 142403 (2014).
- ⁵⁴P. Laczkowski, H. Jaffrès, W. Savero-Torres, J.-C. Rojas-Sánchez, Y. Fu, N. Reyren, C. Deranlot, L. Notin, C. Beigné, J.-P. Attané, L. Vila, J.-M. George, and A. Marty, "Evaluation of spin diffusion length of AuW alloys using spin absorption experiments in the limit of large spin-orbit interactions," *Phys. Rev. B* **92**, 214405 (2015).
- ⁵⁵P. Laczkowski, Y. Fu, H. Yang, J.-C. Rojas-Sánchez, P. Noel, V. T. Pham, G. Zahnd, C. Deranlot, S. Collin, C. Bouard, P. Warin, V. Maurel, M. Chshiev, A. Marty, J.-P. Attané, A. Fert, H. Jaffrès, L. Vila, and J.-M. George, "Large enhancement of the spin Hall effect in Au by side-jump scattering on Ta impurities," *Phys. Rev. B* **96**, 140405 (2017).
- ⁵⁶M. Obstbaum, M. Decker, A. K. Greitner, M. Haertinger, T. N. G. Meier, M. Kronseder, K. Chadova, S. Wimmer, D. Ködderitzsch, H. Ebert, and C. H. Back, "Tuning spin Hall angles by alloying," *Phys. Rev. Lett.* **117**, 167204 (2016).
- ⁵⁷Y. Xu, Y. Yang, H. Xie, and Y. Wu, "Spin Hall magnetoresistance sensor using Au_xPt_{1-x} as the spin-orbit torque biasing layer," *Appl. Phys. Lett.* **115**, 182406 (2019).
- ⁵⁸L. Cheng, X. Wang, W. Yang *et al.*, "Far out-of-equilibrium spin populations trigger giant spin injection into atomically thin MoS₂," *Nat. Phys.* **15**, 347–351 (2019).
- ⁵⁹R. B. Wilson, Y. Yang, J. Gorchon, C.-H. Lambert, S. Salahuddin, and J. Bokor, "Electric current induced ultrafast demagnetization," *Phys. Rev. B* **96**, 045105 (2017).
- ⁶⁰Q. Zhang, Z. Luo, H. Li, Y. Yang, X. Zhang, and Y. Wu, "Terahertz emission from anomalous Hall effect in a single-layer ferromagnet," *Phys. Rev. Appl.* **12**, 054027 (2019).
- ⁶¹C. Cerqueira, J. Y. Qin, H. Dang, A. Djéffal, J.-C. L. Breton, M. Hehn, J.-C. Rojas-Sánchez, X. Devaux, S. Sui, S. Migot, P. Schieffer, J.-G. Mussot, P. Łaczkowski, A. Anane, S. Petit-Watelot, M. Stoffel, S. Mangin, Z. Liu, B. W. Cheng, X. F. Han, H. Jaffrès, J.-M. George, and Y. Lu, "Evidence of pure spin-current generated by spin pumping in interface-localized states in hybrid metal–silicon–metal vertical structures," *Nano Lett.* **19**, 90–99 (2019).
- ⁶²R. Iguchi and E. Saitoh, "Measurement of spin pumping voltage separated from extrinsic microwave effects," *J. Phys. Soc. Jpn.* **86**, 011003 (2017).
- ⁶³L. Bocklage, "Model of THz magnetization dynamics," *Sci. Rep.* **6**, 22767 (2016).
- ⁶⁴L. Bocklage, "Coherent THz transient spin currents by spin pumping," *Phys. Rev. Lett.* **118**, 257202 (2017).
- ⁶⁵P. Maldonado, K. Carva, M. Flammer, and P. M. Oppeneer, "Theory of out-of-equilibrium ultrafast relaxation dynamics in metals," *Phys. Rev. B* **96**, 174439 (2017).
- ⁶⁶M. Battiato, K. Carva, and P. M. Oppeneer, "Superdiffusive spin transport as a mechanism of ultrafast demagnetization," *Phys. Rev. Lett.* **105**, 027203 (2010).
- ⁶⁷M. Battiato, K. Carva, and P. M. Oppeneer, "Theory of laser-induced ultrafast superdiffusive spin transport in layered heterostructures," *Phys. Rev. B* **86**, 024404 (2012).
- ⁶⁸T. Valet and A. Fert, "Theory of the perpendicular magnetoresistance in magnetic multilayers," *Phys. Rev. B* **48**, 7099–7113 (1993).
- ⁶⁹S. Kaltenborn, Y.-H. Zhu, and H. C. Schneider, "Wave-diffusion theory of spin transport in metals after ultrashort-pulse excitation," *Phys. Rev. B* **85**, 235101 (2012).

- ⁷⁰D. M. Nenzo, R. Binder, and H. C. Schneider, "Simulation of hot-carrier dynamics and terahertz emission in laser-excited metallic bilayers," *Phys. Rev. Appl.* **11**, 054083 (2019).
- ⁷¹O. Gunnarsson, O. Jepsen, and O. K. Andersen, "Self-consistent impurity calculations in the atomic-spheres approximation," *Phys. Rev. B* **27**, 7144–7168 (1983).
- ⁷²I. Turek, V. Drchal, J. Kudrnovsky, M. Sob, and P. Weinberger, *Electronic Structure of Disordered Alloys, Surfaces and Interfaces* (Springer, New York, 1997).
- ⁷³D. Pashov, S. Acharya, W. R. L. Lambrecht, J. Jackson, K. D. Belashchenko, A. Chantis, F. Jamet, and M. van Schilfgaarde, "Questaal: A package of electronic structure methods based on the linear muffin-tin orbital technique," [arXiv:1907.06021](https://arxiv.org/abs/1907.06021) (2019).
- ⁷⁴U. von Barth and L. Hedin, "A local exchange-correlation potential for the spin polarized case. i," *J. Phys. C: Solid State Phys.* **5**, 1629–1642 (1972).
- ⁷⁵K. M. Schep, J. van Hoof, P. J. Kelly, G. E. W. Bauer, and J. E. Inglesfield, "Interface resistances of magnetic multilayers," *Phys. Rev. B* **56**, 10805–10808 (1997).
- ⁷⁶T. H. Dang, Q. Barbedienne, D. Q. To, E. Rongione, N. Reyren, F. Godel, S. Collin, J. M. George, and H. Jaffrès, "Anomalous Hall effect in 3d/5d multilayers mediated by interface scattering and nonlocal spin conductivity," *Phys. Rev. B* **102**, 144405 (2020).
- ⁷⁷J. Wiczkorek, A. Eschenlohr, B. Weidtmann, M. Rösner, N. Berggaard, A. Tarasevitch, T. O. Wehling, and U. Bovensiepen, "Separation of ultrafast spin currents and spin-flip scattering in Co/Cu(001) driven by femtosecond laser excitation employing the complex magneto-optical Kerr effect," *Phys. Rev. B* **92**, 174410 (2015).
- ⁷⁸J. Bass and W. P. Pratt, "Spin-diffusion lengths in metals and alloys, and spin-flipping at metal/metal interfaces: An experimentalist's critical review," *J. Phys.: Condens. Matter* **19**, 183201 (2007).
- ⁷⁹D. Gall, "Electron mean free path in elemental metals," *J. Appl. Phys.* **119**, 085101 (2016).
- ⁸⁰V. P. Zhukov, E. V. Chulkov, and P. M. Echenique, "Lifetimes and inelastic mean free path of low-energy excited electrons in Fe, Ni, Pt, and Au: *Ab initio* GW+T calculations," *Phys. Rev. B* **73**, 125105 (2006).
- ⁸¹R. Freeman, A. Zholud, Z. Dun, H. Zhou, and S. Urazhdin, "Evidence for Dyakonov-Perel-like spin relaxation in Pt," *Phys. Rev. Lett.* **120**, 067204 (2018).
- ⁸²A. Fert and S.-F. Lee, "Theory of the bipolar spin switch," *Phys. Rev. B* **53**, 6554–6565 (1996).
- ⁸³J. Lloyd-Hughes and E. Saitoh, "A review of the terahertz conductivity of bulk and nano-materials," *J. Infrared, Millimeter, Terahertz Waves* **33**, 871–925 (2012).
- ⁸⁴L. Zhu, D. C. Ralph, and R. A. Buhrman, "Spin-orbit torques in heavy-metal ferromagnet bilayers with varying strengths of interfacial spin-orbit coupling," *Phys. Rev. Lett.* **122**, 077201 (2019).
- ⁸⁵J. P. Perdew, K. Burke, and M. Ernzerhof, "Generalized gradient approximation made simple," *Phys. Rev. Lett.* **77**, 3865–3868 (1996).
- ⁸⁶For the sake of clarity, we adopt a spin-independent notation of the diffusion coefficient \bar{D} and scattering time $\bar{\tau}$. In this approximation, we suppose the respective spin-dependent quantities to be very close to one another (which is the case in our model), i.e., $\tau_{\uparrow} \simeq \tau_{\downarrow}$ and $D_{\uparrow} \simeq D_{\downarrow}$. Their respective sum and product shall be non-zero.
- ⁸⁷W. Zhang, V. Vlaminck, J. E. Pearson, R. Divan, S. D. Bader, and A. Hoffmann, "Determination of the Pt spin diffusion length by spin-pumping and spin Hall effect," *Appl. Phys. Lett.* **103**, 242414 (2013).